The mycobacterial ABC transporter IrtAB employs a membrane-facing crevice for siderophore-mediated iron uptake

Check for updates

Imre Gonda [1], Simona Sorrentino[2], Laura Galazzo [3], Nicolas P. Lichti [1], Fabian M. Arnold[1], Ahmad R. Mehdipour[4], Enrica Bordignon [3] ✉ & Markus A. Seeger [1,5] ✉

The mycobacterial ABC transporter IrtAB features an ABC exporter fold, yet it imports iron-charged siderophores called mycobactins. Here, we present extensive cryo-EM analyses and DEER measurements, revealing that IrtAB alternates between an inward-facing and an outward-occluded conformation, but does not sample an outward-facing conformation. When IrtAB is locked in its outward-occluded conformation in nanodiscs, mycobactin is bound in the middle of the lipid bilayer at a membrane-facing crevice opening at the heterodimeric interface. Mutations introduced at the crevice abrogate mycobactin import and in corresponding structures, the crevice is collapsed. A conserved triple histidine motif coordinating a zinc ion is present below the mycobactin binding site. Substitution of these histidine residues with alanine results in a decoupled transporter, which hydrolyzes ATP, but lost its capacity to import mycobactins. Our data suggest that IrtAB imports mycobactin via a credit-card mechanism in a transport cycle that is coupled to the presence of zinc.

Iron is an essential micronutrient that is locked away by host organisms to suppress the growth of pathogenic invaders[1]. Microorganisms such as the causative agent of tuberculosis (TB), *Mycobacterium tuberculosis*, have therefore evolved highly specific iron scavenging systems relying on secreted small molecules called siderophores, which bind ferric iron (Fe^{3+}) with extraordinarily high affinity[2]. In mycobacteria, the most important class of siderophores are called mycobactins, which are produced either in a secreted form called carboxymycobactin (cMBT) or a membrane-bound form called mycobactin (MBT)[3]. MBT and cMBT share the same iron-binding core and only differ in their modification with either a shorter dicarboxylate (cMBT) or a longer fatty acid (MBT). Biosynthesis of mycobactins occurs in the cytoplasm, and they are exported to the periplasm via the proton-driven transporters MmpL4 and MmpL5 in a process that also requires the respective accessory

protein MmpS4 and MmpS5[4–6]. Proteins facilitating mycobactin-transport across the outer mycobacterial membrane are yet to be identified. The final steps of the mycobactin cycle are the uptake of iron-loaded Fe-(c)MBT across the inner membrane followed by the reductive release of ferrous iron (Fe^{2+}) in the cytoplasm, processes that are both accomplished by the unusual ABC transporter IrtAB[7,8].

IrtAB belongs to the ubiquitous ATP-binding cassette (ABC) transporter family[9]. Typical ABC transporters consist of two transmembrane domains (TMDs), which are highly variable at the structural and sequence level, and conserved nucleotide-binding domains (NBDs). Substrate translocation across the lipid bilayer is mediated by the TMDs and is coupled to the movement of the NBDs, which dimerize and disengage as a result of ATP binding and hydrolysis, respectively. In the case of IrtAB, the entire transporter is composed of

[1]Institute of Medical Microbiology, University of Zurich, Zurich, Switzerland. [2]Center for Microscopy and Image Analysis, University of Zurich, Zurich, Switzerland. [3]Department of Physical Chemistry, University of Geneva, Geneva, Switzerland. [4]UGent Center for Molecular Modelling, Ghent University, Ghent, Belgium. [5]National Center for Mycobacteria, University of Zurich, Zurich, Switzerland. ✉e-mail: enrica.bordignon@unige.ch; m.seeger@imm.uzh.ch

two polypeptide chains (IrtA and IrtB), which heterodimerize to build the fully assembled transporter composed of two TMDs and two NBDs[8]. As a specialty, the N-terminus of the IrtA chain encodes for a siderophore interaction domain (SID), which is located in the cytoplasm and mediates mycobactin reduction and iron release[8,10].

IrtAB has been initially identified to play a key role in the mycobactin pathway based on the observation that its transcription is under the control of the iron regulator protein IdeR[11], and its genetic deletion resulted in a pronounced virulence defect in a TB mouse model[7]. Further work revealed that IrtAB imports iron-bound mycobactin into the cytoplasm[10]. This function, however, appeared puzzling since IrtAB belongs to the subfamily of type I ABC exporters (also categorized as type IV ABC transporter), which are generally known to export substrates such as for example, drugs out of the cell[12]. Our lab solved a combined X-ray and cryo-EM structure of IrtAB of the thermophilic species *Mycobacterium thermoresistibile*, which confirmed the ABC exporter fold[8]. Functional elucidation with purified and membrane-reconstituted IrtAB showed that the transporter is capable of Fe-cMBT import in proteoliposomes in an ATP-dependent fashion[8]. The cryo-EM structure of inward-facing (IF) IrtAB revealed that the SID is ideally positioned to reduce MBT[8]. Recently, an outward-occluded (OF_occl) cryo-EM structure of IrtAB of *M. tuberculosis* (MTB) was described, which was obtained by introducing glutamate to glutamine substitutions at the Walker B motifs of IrtA and IrtB[13].

Here, we thoroughly characterized the unusual ABC transporter IrtAB by determining a cryo-EM structure in a complex with Fe-MBT and by combining functional and biochemical assays with DEER measurements to formulate a novel mycobactin transport mechanism.

Results

Cryo-EM analysis of IrtAB in nanodiscs
IrtAB of *M. thermoresistibile* (MTHERM) exhibits robust ATPase activity in nanodiscs[8]. Full-length wild-type (WT)-IrtAB was therefore reconstituted in nanodiscs and analyzed by cryo-EM. In the presence of ATP-γ-S-Mg, we determined a cryo-EM structure of inward-facing IrtAB at a global resolution of 3.67 Å (dataset #1, Supplementary Table S1 and Supplementary Fig. 1) and observed the binding of two ATP-γ-S molecules at the respective nucleotide binding sites (Supplementary Fig. 2a). The inward-facing cryo-EM structure was found to be highly similar to the previously solved X-ray structure of MTHERM-IrtAB determined with the transporter purified in β-DDM[8] and the cryo-EM structure of inward-facing MTB-IrtAB determined in digitonin[13] (Supplementary Fig. 3). This can be explained by interactions of conserved hydrophobic C-terminal residues of the IrtB-NBD with the IrtA-NBD, which restrict the conformational freedom of the NBDs (Supplementary Fig. 4a).

Upon incubation with ATP-Mg and vanadate, cryo-EM analysis (dataset #2, Supplementary Table S1 and Supplementary Fig. 5) revealed the structure of an outward-occluded (OF_occl) conformation determined at a global resolution of 3.14 Å (Fig. 1). Particles corresponding to the IF conformation were found as well, but could not be resolved to high resolution (Supplementary Fig. 5). We observed density for two ADP-vanadate molecules at the fully closed NBD dimer interface (Supplementary Fig. 2b). The extracellular wings at the TMDs remained closed, as first described for the ABC transporter McjD[14] and later for MsbA[15,16], TmrAB[17], AtAtm3[18] and PCAT1[19] (Supplementary Fig. 3). As a consequence, the TMDs surround a large internal cavity (Fig. 1c) that is sealed from both sides of the membrane, enclosing a volume of 5005 Å³, which is large enough to fit up to two iron bound mycobactins simultaneously (Supplementary Fig. 6). Of note, the recently determined OF_occl structures of MTB-IrtAB and yersiniabactin importer YbtPQ feature a similarly sized cavity[13,20].

Cryo-EM analysis of IrtAB in LMNG
Considering that nanodiscs might bias the conformational ensemble of ABC transporters[16], the purification protocol was optimized using

LMNG as a detergent. In contrast to IrtAB purified in β-DDM or β-DM[8], LMNG-purified IrtAB exhibits ATPase activity, which was stimulated up to 24-fold by MBT and up to 5-fold by cMBT (Supplementary Fig. 2e). Full-length IrtAB in LMNG was analyzed by cryo-EM in the presence or absence of ATP-Mg vanadate. Again, we observed the IF conformation in the absence of nucleotides (global resolution of 3.42 Å) and the OF_occl conformation in the presence of ATP-Mg vanadate (global resolution of 3.23 Å) (Fig. 1b and Supplementary Fig. 7, 8). However, no additional conformations were identified. Distance comparisons between conserved residues in the coupling helices of the TMDs and the NBDs showed that the structures determined in LMNG differed only marginally when compared to their respective counterparts determined in nanodiscs (Supplementary Fig. 3).

The SID is highly mobile in outward-occluded IrtAB
The four structures determined for full-length WT-IrtAB in nanodiscs and LMNG allowed us to analyze the flexibility of the SID in the context of different membrane mimics and alternate conformations. When IrtAB was purified in LMNG, the SID was generally better resolved than upon reconstitution in nanodiscs (Fig. 1b). Likewise, density for the SID was found to be less defined when IrtAB adopts its outward-occluded conformation. We performed a 3D variability analysis using the inward-facing structure determined in LMNG and observed a swinging movement of the SID along the membrane in front of the inward-facing opening of the IrtA chain (Supplementary Fig. 4b).

Mycobactin binds at a membrane-facing crevice at the heterodimer interface
The cryo-EM analyses of full-length WT-IrtAB were mostly carried out in the presence of Fe-MBT or Fe-cMBT at a concentration that results in maximal stimulation of ATPase activity (Supplementary Table S1). However, in these datasets, we were unable to identify non-proteinaceous cryo-EM density corresponding to mycobactin. Instead, we observed the binding of a lipid of unclear identity (in case of nanodisc-reconstituted IrtAB) or an LMNG molecule to a hydrophobic pocket located at the periplasmic end of a crevice spanning the almost the heterodimer interface between helices TMH2^IrtA and TMH5^IrtB of OF_occl IrtAB (Fig. 1b). The membrane-facing crevice and its lipid/detergent-filled hydrophobic pocket at the periplasmic end is a unique feature of OF_occl IrtAB; in inward-facing IrtAB, the pocket is closed and devoid of bound lipid (Figs. 1b, 2a).

We suspected that the flexible SID limits cryo-EM map resolution, and made a IrtAB construct lacking the SID. ATPase activity measurements with full-length IrtAB and IrtABΔSID purified in LMNG revealed that the deletion of the SID causes only minor changes in the maximally stimulated ATPase activity (Supplementary Fig. 2g), which differs within the typical error range of protein concentration determination underlying such assays. In order to trap IrtABΔSID more efficiently in its NBD-closed conformation, we mutated the Walker B glutamate of both NBDs into glutamine (E815Q^IrtA-E493Q^IrtB, henceforth denoted the 2xEQ mutation), which has been shown previously to render IrtAB inactive[8]. Purified 2xEQ-IrtABΔSID was then reconstituted into nanodiscs and ATP-Mg as well as Fe-MBT were added before grid preparation (dataset #5, Supplementary Table 1 and Supplementary Fig. 9). The same preparation without added Fe-MBT served as negative control (dataset #6, Supplementary Table 1 and Supplementary Fig. 10). In these samples, we only found 2D and 3D classes corresponding to the outward-occluded conformation, which could be further split into two similarly sized subclasses (Supplementary Fig. 9). In the samples with mycobactin present, one of this subclasses featured a strong non-proteinaceous density close to a membrane-facing crevice present at the heterodimer interface between helices TMH2^IrtA and TMH5^IrtB of OF_occl IrtAB (Fig. 2b). Fe-MBT could be placed unambiguously into the density. Importantly, the density
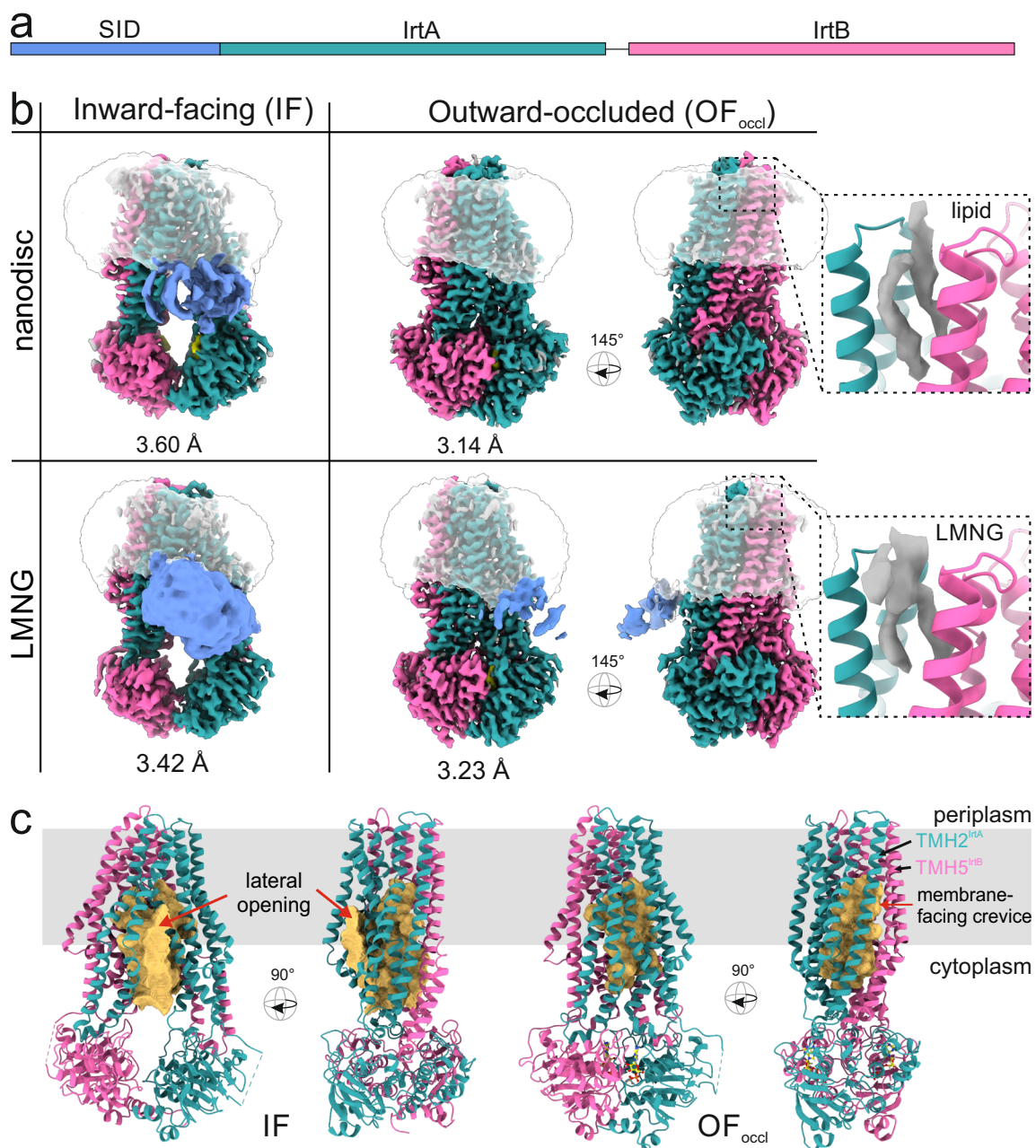
Fig. 1 | Conformational states of IrtAB. a Domain organization of IrtAB. The siderophore interaction domain (SID, blue) is N-terminally positioned to IrtA (teal). IrtB (pink) forms a separate open reading frame. **b** Cryo-EM maps of full-length IrtAB reconstituted in nanodisc or purified in LMNG detergent. Inward-facing (IF) and outward-occluded (OF$_{occl}$) maps were determined from distinct datasets. At the periplasmic side of OF$_{occl}$ IrtAB, a non-proteinaceous density (contoured at 6 σ) is observed, which likely corresponds to a phospholipid (nanodisc sample) or an LMNG molecule (detergent sample). The SID (blue density) was generally less well resolved. **c** The IF cavity is accessible from the inner leaflet of the lipid bilayer. The OF$_{occl}$ conformation features a large cavity that is sealed from both sides of the membrane. In the OF$_{occl}$ conformation, a lateral membrane-facing crevice spanning across the whole lipid bilayer is formed between TMH2^{IrtA} and TMH5^{IrtB}.

was not present in the control samples prepared in parallel devoid of mycobactin (Supplementary Fig. 11). Relative to the lipid bilayer, the mycobactin binding site is located at the level of the hydrophobic core (Fig. 2). Hence, during sample preparation, Fe-MBT most likely entered the crevice at the periplasmic entrance and slit down to its binding site with its bulky head group partially exposed to the lipid bilayer and partially shielded by the crevice formed between TMH2^{IrtA} and TMH5^{IrtB}. Curiously, an additional density featuring an α-helix not stemming from IrtAB was found to interact with Fe-MBT, which most likely corresponds to a part of the MSP protein stabilizing the lipid patch of the nanodiscs (Fig. 2b). The

same density feature was also found the control dataset devoid of Fe-MBT (Supplementary Fig. 11). It is possible that this α-helix blocks Fe-MBT during its passage and was necessary to trap the substrate at this position.

With a buried surface area of 486 Å² (determined by PDBePISA server), IrtAB interacts extensively with Fe-MBT mostly via van der Waals contacts (Fig. 2c). A notable residue is Q249^{IrtB}, whose side chain is also engaged in a hydrogen bond with Fe-MBT. While the density for the iron-chelating moiety of Fe-MBT is strong, the tail of Fe-MBT is much less resolved, and thus assumes an ensemble of different conformations.
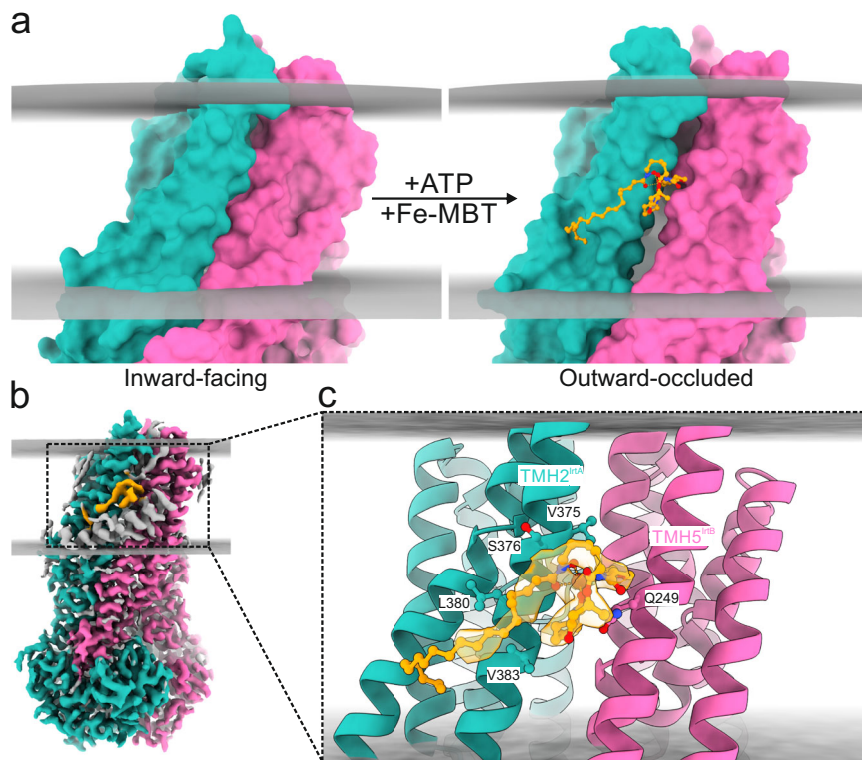
Fig. 2 | Structure of IrtAB in complex with mycobactin. a Cryo-EM structures of inward-facing IrtAB (left panel, Dataset #1, PDB 9FXC) and outward-occluded 2xEQ-IrtAB (right panel, Dataset #5, PDB 9FW3), both obtained in nanodiscs. Shown are the surface representations of the modeled structures. IrtA is colored teal, IrtB magenta, and bound Fe-MBT in orange sticks. The membrane boundaries are indicated in gray planes. **b** Cryo-EM map of outward-occluded 2xEQ-IrtAB (Dataset #5, PDB 9FW3) with non-proteinaceous densities contoured at 5 σ and colored in orange (accounted for Fe-MBT) or in gray (likely stemming from lipids and the nanodiscs belt protein). **c** Detailed depiction of Fe-MBT binding site at the membrane-facing crevice formed between TMH2^{IrtA} and TMH5^{IrtB}. Side chains interacting with Fe-MBT are highlighted as sticks.

Mutational analysis of the mycobactin binding site

To functionally analyze the mycobactin binding site, we mutated Q249^{IrtB} to alanine, leucine, phenylalanine, or arginine. All four variants could be purified in LMNG with yields and size exclusion chromatography profiles similar to WT-IrtAB. We measured ATPase activities of the purified variants in the presence and absence of 5 μM Fe-MBT, a mycobactin concentration at which WT-IrtAB is strongly stimulated (Fig. 3 and Supplementary Fig. 2g, h). Strikingly, the basal ATPase activities of variants Q249A^{IrtB}, Q249L^{IrtB}, and Q249F^{IrtB} were highly elevated as compared to WT-IrtAB, and could not be further stimulated by Fe-MBT (Fig. 3b). Of further note, stimulated ATPase activities of Q249L^{IrtB} and Q249F^{IrtB} were almost around twice as high as those of WT-IrtAB. Our data suggest that Q249^{IrtB}, as found in WT-IrtAB, triggers ATPase activity only if it interacts with mycobactin, and accordingly suppresses ATPase activity when the natural substrate is absent. This "break" is evidently released when Q249^{IrtB} is substituted by alanine, leucine, or phenylalanine. By stark contrast, the Q249R^{IrtB} variant exhibited ATPase activities very similar to WT-IrtAB.

Next, the variants were used to complement a previously described *M. smegmatis* triple knockout (TKO) strain, which lacks two genes for siderophore biosynthesis and its endogenous *irtAB* gene[8]. As controls, complementation was carried out with WT-IrtAB (homolog from *M. thermoresistibile* throughout) and ATPase-deficient 2xEQ-IrtAB. Cells were grown under low iron conditions and radioactively labeled $^{55}Fe^{3+}$-cMBT was added before incubating the cells for 30 min at 37 °C to facilitate IrtAB-mediated cMBT uptake (Fig. 3c and Supplementary Fig. 12, where further details are provided). In this assay, a clear difference in terms of cMBT uptake between cells complemented with WT-IrtAB and 2xEQ-IrtAB is consistently observed. However, cells complemented with 2xEQ-IrtAB exhibit basal uptake levels, which we

previously showed to occur independently from IrtAB via an alternative uptake pathway[8] (Supplementary Fig. 12). Cells complemented with the variant Q249A^{IrtB} exhibited near WT-IrtAB transport activity, while variants Q249L^{IrtB} and Q249F^{IrtB} showed a partial loss of cMBT uptake (Fig. 3c). Hence, the polar interactions between Q249^{IrtB} and Fe-MBT do not appear to be critically important for transport.

Intriguingly, the variant Q249R^{IrtB} completely lost its capacity to import Fe-cMBT and only exhibited the IrtAB-independent uptake seen also for ATPase deficient 2xEQ-IrtAB (Fig. 3c). This finding was puzzling, because in terms of basal and stimulated ATPase activities, Q249R^{IrtB} is very similar to WT-IrtAB. Hence, the single Q249R^{IrtB} substitution resulted in a decoupled transporter, which hydrolyzes ATP, but lost its capacity to import mycobactins. To gain structural insights, the Q249R^{IrtB} substitution was introduced into the 2xEQ-IrtAB background for cryo-EM analyses. In nanodiscs, cryo-EM analyses of this variant were unfortunately not successful. Therefore, we determined its structure in LMNG in the presence of ATP-Mg and Fe-MBT (dataset #7, Supplementary Table 1 and Supplementary Fig. 13). The best-resolved map revealed local conformational rearrangements resulting in a collapse of the entire membrane-facing crevice (Fig. 3d). Importantly, this striking difference cannot be explained by differences between IrtAB prepared in nanodiscs or LMNG, because the OF$_{occl}$ conformation of other cryo-EM structures determined in LMNG feature an open membrane-facing crevice (Fig. 1b).

Mutational analysis of the membrane-facing crevice

Fe-MBT likely slides along the membrane-facing crevice formed at the IrtA/IrtB interface to reach its binding site as observed in the mycobactin-bound structure of OF$_{occl}$ IrtAB (Fig. 2). At its periplasmic entry site, the crevice is filled with a lipid, bound to a hydrophobic
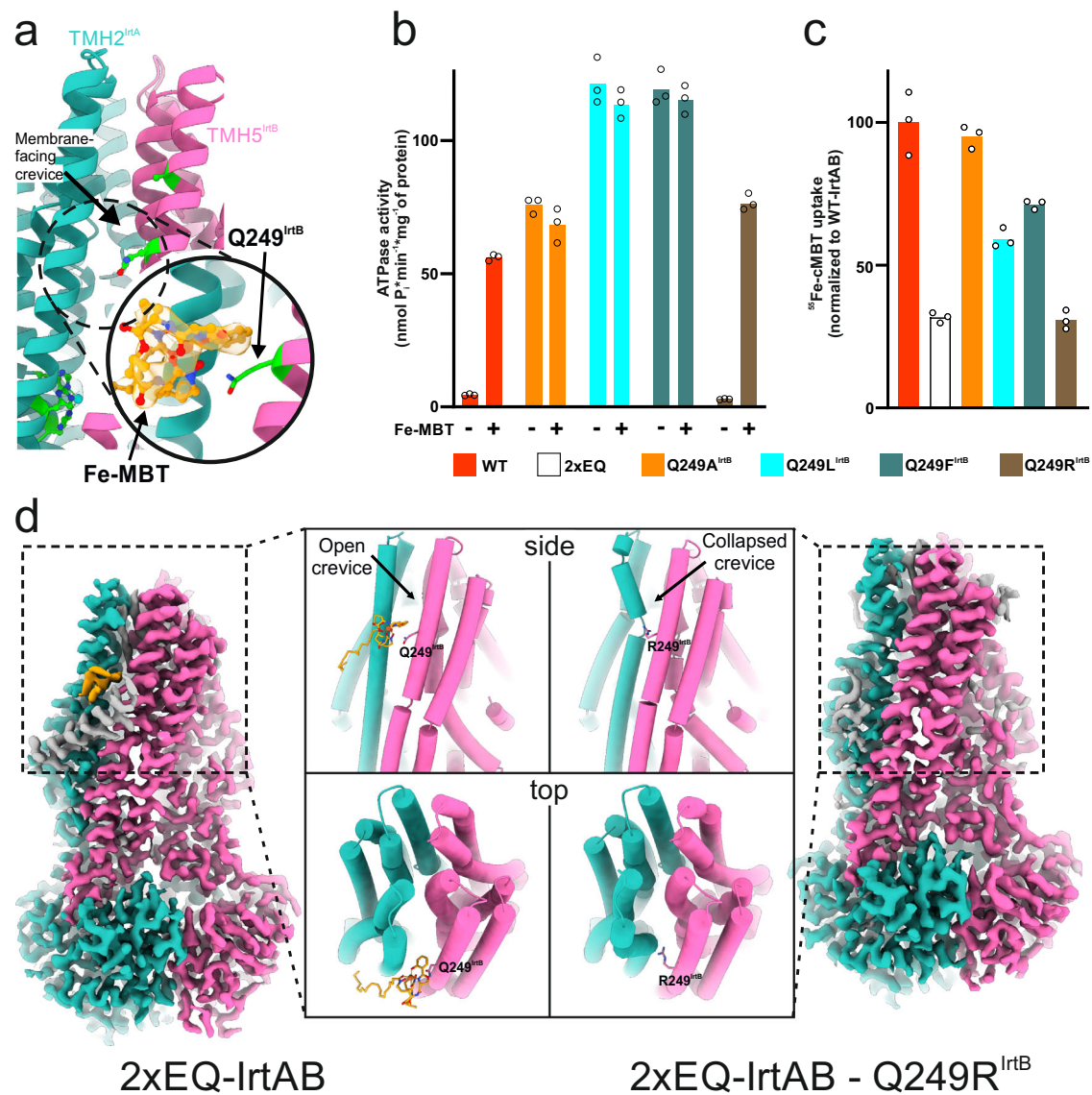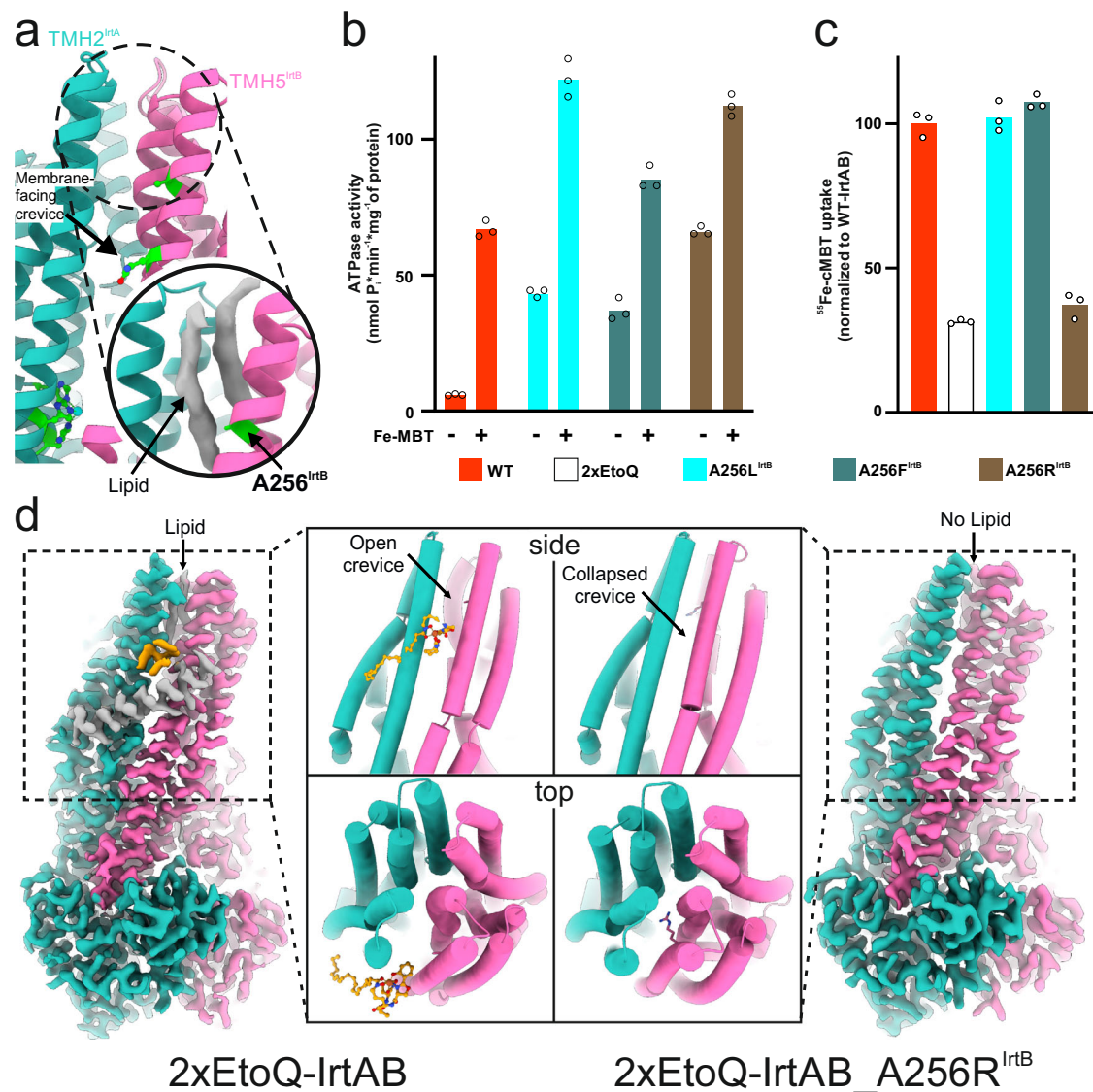
Fig. 3 | Mutational analysis of mycobactin binding site. a The membrane-facing crevice opens up between TMH2^{IrtA} and TMH5^{IrtB} in the OF$_{occl}$ conformation. IrtA is colored teal, and IrtB is magenta. In the middle part of the crevice, Fe-MBT is bound (Dataset #5, PDB 9FW3, OF$_{occl}$ structure). Residue Q249^{rtB} interacts with Fe-MBT, and was functionally characterized. **b** ATPase activity of purified Q249A^{IrtB}, Q249L^{IrtB}, Q249F^{IrtB}, and Q249R^{IrtB} variants with WT-IrtAB as control in the presence or absence of 5 μM Fe-MBT. Data points correspond to technical triplicates. **c** In vivo uptake of ^{55}Fe-cMBT in *M. smegmatis* cells unable to produce their own siderophores and lacking the genomic copy of *irtAB*. Cells were complemented with WT-IrtAB (positive control), ATPase-deficient 2xEQ-IrtAB (negative control), and the four mycobactin binding site variants. Note that *M. smegmatis* cells exhibit IrtAB-independent Fe-cMBT uptake. Data points correspond to technical triplicates. **a**, **b** For both functional assays, representative data of at least two biological replicates are shown. Source data are provided as a Source Data file. **d** Structural comparison of Fe-MBT bound 2xEQ-IrtAB (Dataset #5, PDB 9FW3) and the 2xEQ-IrtAB-Q249R^{IrtB} variant (Dataset #7, PDB 9G2S) unable to bind Fe-MBT owing to crevice collapse.

cavity (Fig. 1b). To block Fe-MBT passage at the lower end of the hydrophobic cavity, we mutated A256^{IrtB} into bulky or charged residues, namely leucine, phenylalanine or arginine (Fig. 4a). When purified in LMNG, the three variants exhibited elevated basal ATPase activity, with the A256R^{IrtB} showing more than ten-fold higher ATP hydrolysis than WT-IrtAB (Fig. 4b). The basal activities of the three A256^{IrtB} variants were found to be further stimulated by Fe-MBT. Subsequently, we performed the radioactive ^{55}Fe^{3+}-cMBT uptake assay to assess the transport capacity of the variants. Variants A256L^{IrtB} and A256F^{IrtB} were fully transport-competent (Fig. 4c). In contrast, the variant A256R^{IrtB} completely lost its capacity to import cMBT, hence exhibiting a decoupled transport phenotype akin to the above-described Q249R^{IrtB} variant.

To investigate this finding at the structural level, the A256R^{IrtB} mutation was combined with the ATPase-deficient 2xEQ mutant. While determining a structure in nanodiscs was not successful for this mutant, we achieved to obtaine highly resolved cryo-EM structures in LMNG in the presence of ATP-Mg (dataset #8, Supplementary Table 1 and Supplementary Fig. 14). Data analysis revealed two main classes. The first class closely resembles the OF$_{occl}$ structure of 2xEQ-IrtAB and shows density for the newly introduced R256^{IrtB} residue pointing outward and thereby interrupting the crevice. Density for LMNG was found to be weaker than in other OF$_{occl}$ structures (Supplementary Fig. 15). The second class features the R256^{IrtB} residue pointing towards the occluded cavity (Supplementary Fig. 14). As a consequence, the entire lateral crevice is collapsed (Fig. 4d) and no detergent molecule is

Fig. 4 | Mutational analysis of the membrane-facing crevice. a The membrane-facing crevice opens up between TMH2^{IrtA} and TMH5^{IrtB} in the OF$_{occl}$ conformation. IrtA is colored teal, and IrtB is magenta. In the upper part of the crevice, a hydrophobic pocket is formed, which is occupied with a lipidic moiety (Dataset #5, PDB 9FW3, OF$_{occl}$ structure). Residue A256^{IrtB}, located below the lipid-binding pocket, is shown as a green stick and was functionally characterized. **b** ATPase activity of purified A256L^{IrtB}, A256F^{IrtB}, and A256R^{IrtB} variants with WT-IrtAB as control in the presence or absence of 5 μM MBT. Data points correspond to technical triplicates. **c** In vivo uptake of ^{55}Fe-cMBT in *M. smegmatis* cells unable to produce their own siderophores and lacking the genomic copy of *irtAB*. Cells were complemented with WT-IrtAB (positive control), ATPase-deficient 2xEQ-IrtAB (negative control), and the three lateral crevice variants. Note that *M. smegmatis* cells exhibit IrtAB-independent Fe-cMBT uptake. Data points correspond to technical triplicates. **b, c** For both functional assays, representative data of at least two biological replicates are shown. Source data are provided as a Source Data file. **d** Structural comparison of 2xEQ-IrtAB with bound Fe-MBT (Dataset #5, PDB 9FW3) and 2xEQ-IrtAB_A256R^{IrtB} (Dataset #8, PDB 9G2T, Arg256^{IrtB} pointing to protein inside) unable to bind Fe-MBT and exhibiting a collapsed membrane-facing crevice.

bound at the location where it is present in OF$_{occl}$ structures showing the open crevice (Supplementary Fig. 15).

In conclusion, our structural analyses clearly show that the A256R^{IrtB} mutation blocks the pathway from the periplasm to the mycobactin binding site by either directly interrupting the lateral crevice or indirectly causing large conformational rearrangements that result in a complete crevice collapse.

A conserved triple-histidine (HHH)-motif binds zinc

At the bottom of the lateral crevice, below the mycobactin binding site, we observed a strong non-proteinaceous density in both conformations (Fig. 5a, Supplementary Fig. 16). The density is coordinated by three histidine residues (HHH-motif) that are conserved among mycobacterial homologs of IrtAB (Fig. 5b). An analogous motif is also

present in the yersiniabactin importer YbtPQ[21], with the third histidine being an aspartate (HHD-motif) (Fig. 5b and Supplementary Fig. 16). Based on the chemical environment and the geometrical arrangement, we assumed it is a transition metal ion with a preference for soft Lewis base ligands in a tetrahedral arrangement, i.e., Zn^{2+}, Cd^{2+}, Co^{2+} or Ni^{2+} [22]. To identify the coordinated metal ion, we performed Inductively Coupled Plasma Mass Spectrometry (ICP-MS) analysis with metals extracted from WT-IrtAB or 3xHtoA-IrtAB, in which the three histidines were substituted by alanines to prevent metal coordination. In order to avoid metal cross-contamination, the transporters were purified using a nanobody-functionalized resin capturing IrtAB via the C-terminal GFP-tag, instead of Ni^{2+}-NTA affinity chromatography. In the first ICP-MS experiment, we measured the signals of 75 elements extracted from purified WT-IrtAB and compared them to the buffer control.
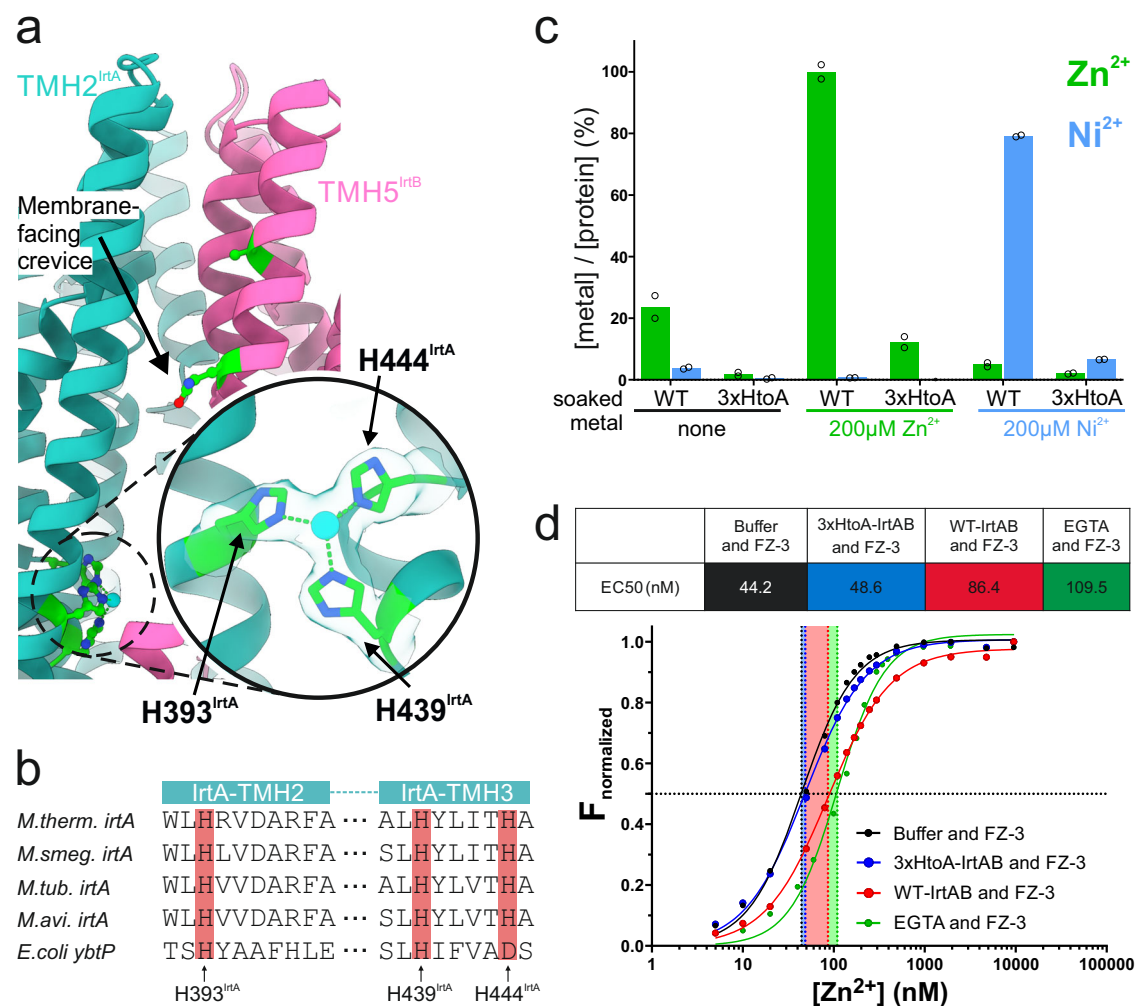
Fig. 5 | Identification of zinc binding motif. a Three histidine residues are localized in the cavity at the bottom of the lateral crevice and coordinate a metal atom. **b** The HHH motif is highly conserved among mycobacterial homologs of IrtAB, and it is also present as a slightly deviant HHD motif in YbtPQ, a yersiniabactin importer from uropathogenic *E. coli.* **c** ICP-MS analysis of WT-IrtAB and 3xHtoA-IrtAB in the absence of added metals or pre-soaked with 200 µM Zn^{2+}- or Ni^{2+}-ions. **d** Zn^{2+}-titration curves using the zinc-sensitive FluoZin-3 (FZ-3) fluorescent probe. FZ-3 concentration was 200 nM for all measurements. Titrations were performed in buffer control or in the presence of equimolar WT-IrtAB (200 nM), 3xHtoA-IrtAB (200 nM), or the strong zinc-chelator EGTA (200 nM). EC_{50} values correspond to the Zn^{2+} concentration at which half-maximal florescence of ZN-3 is reached. Source data are provided as a Source Data file.

Thereby, we discovered that purified WT-IrtAB contains elevated levels of Zn^{2+}- and Ni^{2+}- ions. Next, purified WT-IrtAB or 3xHtoA-IrtAB were incubated with either 200 µM $ZnSO_4$, 200 µM $NiSO_4$, or buffer, and unbound metal was removed using a desalting column. The concentration of the eluting transporter was determined by absorption measurements, and the metal content was quantified by ICP-MS. This experiment confirmed our initial finding that WT-IrtAB carries along Zn^{2+}- and Ni^{2+}- ions during purification and further revealed that metal co-purification does not occur in the 3xHtoA-IrtAB control (Fig. 5c). Upon pre-incubation with $ZnSO_4$ or $NiSO_4$, WT-IrtAB was fully saturated with Zn^{2+}-ions (one Zn^{2+}-ion per IrtAB heterodimer), whereas it could not be completely saturated with Ni^{2+}-ions. We observed background binding of Zn^{2+} and Ni^{2+}-ions to the 3xHtoA-IrtAB control upon pre-incubation, but bound metal concentrations reached only around 10 % of the concentrations bound to WT-IrtAB, clearly demonstrating that the HHH-motif is chiefly responsible for metal binding. In addition, in the case of WT-IrtAB, around 10 % Zn^{2+} remained bound in the Ni^{2+}- soaking experiment, whereas Zn^{2+}- soaking fully replaced Ni^{2+} (Fig. 5c), showing that the HHH-motif prefers to bind Zn^{2+} over Ni^{2+}.

To obtain semi-quantitative insights into the binding affinity for Zn^{2+}, WT-IrtAB, 3xHtoA-IrtAB, and the strong Zn^{2+}-chelator EGTA (reported K_D for Zn^{2+} of 4.5×10^{-10} M[23]) were titrated with increasing concentrations of Zn^{2+} in the presence of FluoZin-3, which becomes fluorescent upon Zn^{2+} chelation and has a reported K_D for Zn^{2+} of 15 nM[24]. First, the Zn^{2+} concentration needed to reach half-maximal fluorescence of 200 nM FluoZin-3 was determined to be 44.2 nM (EC_{50} value) (Fig. 5d). Then, Zn^{2+}-titration curves were recorded wherein 200 nM WT-IrtAB, 3xHtoA-IrtAB or EGTA were present at an equimolar ratio to FluoZin-3. The corresponding EC_{50} of FluoZin-3 for Zn^{2+} shifted to higher values for WT-IrtAB (EC_{50} = 86.4 nM) and EGTA (EC_{50} = 109.5 nM) but was basically unaltered when 3xHtoA-IrtAB was present (EC_{50} = 48.6 nM). Since the EC_{50} increases by a factor of two in the equimolar presence of WT-IrtAB as compared to the buffer control, the affinity of the HHH-motif for Zn^{2+} is in the same range as the one of FluoZin-3 (i.e., double-digit nanomolar) (Fig. 5d).

The HHH-motif is essential for energy coupling
In the next step, we characterized the functional role of the HHH-motif. We found that the MBT-stimulated ATPase activity of the LMNG-purified IrtAB variants was not affected by mutations introduced at the HHH-motif (Fig. 6a). This also demonstrates that mutations in this
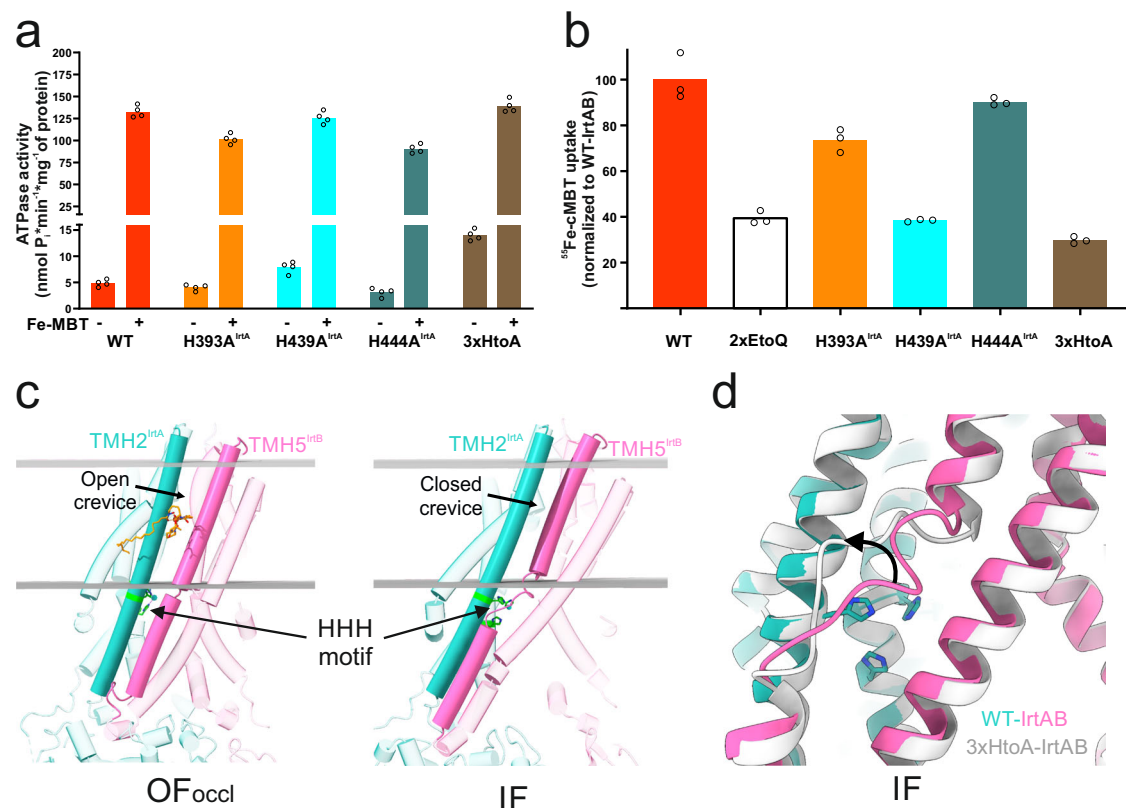
Fig. 6 | Structural and functional analysis of the triple-histidine motif. a ATPase activity of purified HHH-motif variants with WT-IrtAB as a control in the presence or absence of 5 μM MBT. Data points correspond to technical quadruplicates. **b** In vivo uptake of ^{55}Fe-cMBT in *M. smegmatis* cells unable to produce their own siderophores and lacking the genomic copy of *irtAB*. Cells were complemented with WT-IrtAB (positive control), ATPase-deficient 2xEQ IrtAB (negative control), and the individual and combined HHH-motif variants. Note that *M. smegmatis* cells exhibit IrtAB-independent Fe-cMBT uptake. Data points correspond to technical triplicates. **b, c** For both functional assays, representative data of at least two biological replicates are shown. Source data are provided as a Source Data file. **c** Structures of WT-IrtAB under ATP turnover conditions (dataset #9) with Fe-MBT (orange sticks) placed where it was found in nanodiscs (dataset #5) for reference. The HHH motif (green) is highlighted in sticks and the membrane boundaries are indicated in gray planes. **d** Superimposition of inward-facing 3xHtoA-IrtAB (gray, dataset #11) with inward-facing WT-IrtAB (colored, dataset #9).

conserved motif did not affect protein folding. Curiously, the H439A^{IrtA} variant and even more so the 3xHtoA variant showed slightly elevated basal ATPase activities (Fig. 6a). We then performed an in vivo uptake assay with radioactively labeled ^{55}Fe-cMBT in *M. smegmatis* (Fig. 6b). The H444A^{IrtA} variant was fully capable of mycobactin import, which can be explained by the conservation pattern of the HHH-motif because the third histidine is the least conserved and appears as an aspartate in YbtPQ[21]. In contrast, the single variant H393A^{IrtA} exhibited a partial loss of transport activity, while the single variant H439A^{IrtA}, as well as the 3xHtoA variant, lost their ability to import ^{55}Fe^{3+}-cMBT. Hence, disruption of the zinc coordination motif decouples ATP hydrolysis from mycobactin import.

Conformational landscape under ATP turnover conditions

To potentially detect additional conformations, we performed cryo-EM analysis of IrtAB under ATP turnover conditions. To this end, we pre-incubated LMNG-purified WT-IrtABΔSID (20 μM) with ATP-Mg (2 mM) in the presence or absence of Fe-MBT (20 μM) at 25 °C for 30 s before grid freezing and recorded two large cryo-EM datasets (datasets #9 and #10, Supplementary Table 1 and Supplementary Figs. 17, 18). Regardless of whether Fe-MTB was present or not, the cryo-EM analysis only revealed the IF and the OF$_{occl}$ conformations to be present. The corresponding density maps reached global resolutions of 3.21-3.76 Å and 2.78-3.00 Å, respectively. When examining the densities of the bound nucleotides of the OF$_{occl}$ structure in more detail, the γ-phosphate of ATP was clearly found to be present, suggesting that it

represents a pre-hydrolysis state (Supplementary Fig. 2d). In both datasets, the number of particles corresponding to the OF$_{occl}$ conformation was higher than the number of particles corresponding to the IF conformation, clearly showing that the OF$_{occl}$ conformation is populated under hydrolysis conditions (Supplementary Fig. 19). The high number of particles corresponding to the OF$_{occl}$ conformation, i.e., 402'468 and 283'513 for the Fe-MBT and the mycobactin-free dataset, respectively (Supplementary Table 1), would have made it highly feasible to detect the structurally related OF$_{open}$ conformation, but we did not observe it.

Cryo-EM structure of 3xHtoA-IrtAB under turnover conditions

To obtain molecular insights into the uncoupled transport phenotype of 3xHtoA-IrtAB, we performed a cryo-EM analysis using the LMNG-purified, SID-less construct in the presence of 20 μM MBT under turnover condition (dataset #11, Supplementary Table 1 and Supplementary Fig. 20), resulting in maps at global resolutions of 3.2 Å and 3.0 Å for IF and OF$_{occl}$ conformations, respectively (Fig. 6c). Intriguingly, the IF/OF$_{occl}$ equilibrium of 3xHtoA-IrtAB is prominently shifted towards the IF conformation as compared to WT-IrtAB (Supplementary Fig. 19). Compared to the WT-IrtAB sample analyzed under the same experimental conditions (dataset #10), the OF$_{occl}$ models are basically identical (RMSD: 0.453 Å across 1126 residues), apart from the mutated residues. By contrast, we noted a fine difference between the nearly identical IF structures, namely a rearrangement of the unwound stretch of TMH5^{IrtB} and concomitant detachment from the 3xHtoA

motif (Fig. 6d). Of note, TMH5[IrtB] is part of the domain swap helices which are prominently broken in the IF structure of IrtAB, but straighten during the transition to the OF[occl] conformation, thereby representing one of the most dynamic regions of IrtAB (Supplementary Fig. 21). Further, TMH5[IrtB] together with TMH2[IrtA] delineates the lateral crevice that opens up during the IF-OF[occl] transition (Fig. 2). Our structural analysis of the 3xHtoA variant therefore suggests an allosteric coupling of the HHH-motif with dynamic events occurring at the lateral crevice that are essential for mycobactin import.
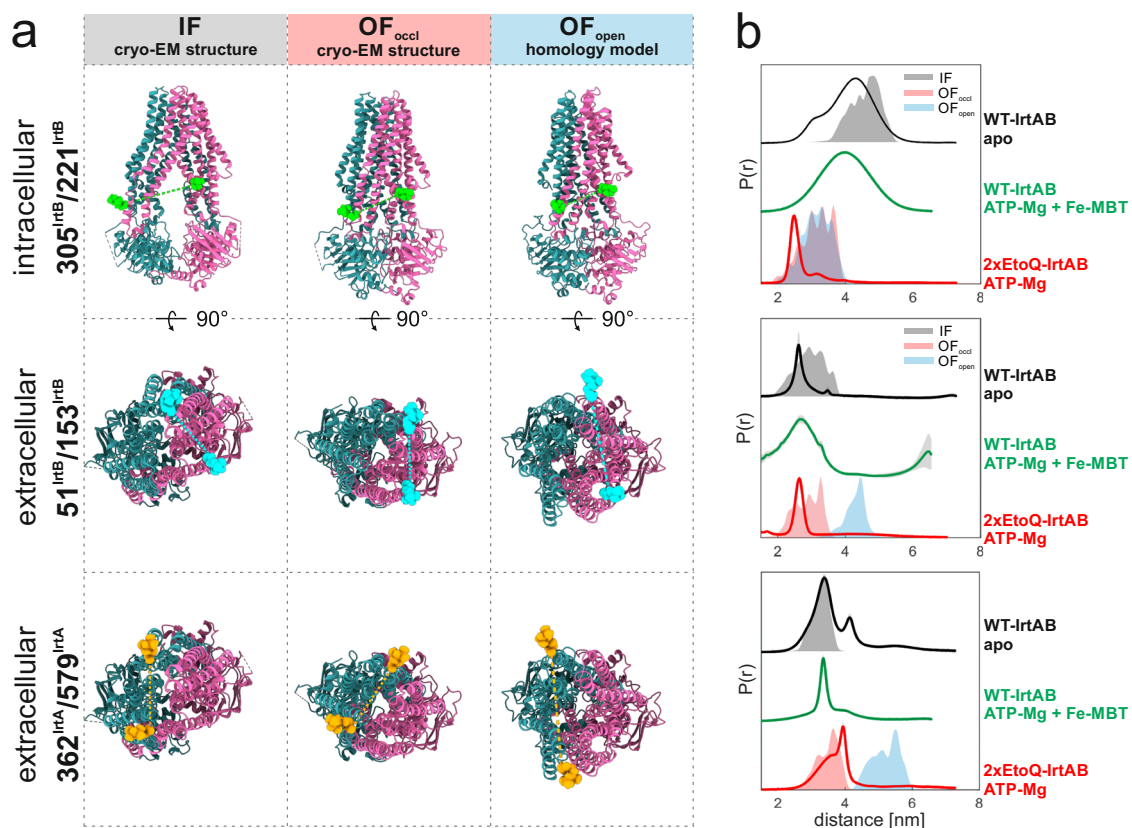
DEER analyses of IrtAB

To study the conformational space of IrtAB by an orthogonal method, we performed DEER measurements on selected spin-labeled variants. We created three pairs of cysteine mutants to be labeled with the paramagnetic nitroxide spin label MTSL using the program MMM to simulate inter-label distances[25] on the IF and OF[occl] structures of IrtAB as well as on an IrtAB homology model based on OF[open] TM287/288 (PDB: 6QUZ)[26]. Two spin-labeling pairs were placed at the periplasmic side on TMH1[IrtA] and TMH3[IrtA] or TMH1[IrtB] and TMH6[IrtB] (Fig. 7). The inter-spin distances of these pairs are expected to remain largely constant during the transition from the IF to the OF[occl] conformation, but would become around 20 Å longer in the OF[open] conformation if the extracellular wings open up. As a control, an intracellular spin-labeling pair was placed on TMH5[IrtB] and TMH6[IrtB]. This pair is expected to become around 20 Å shorter when IrtAB transits from the IF to the OF[occl] conformation but is invariant regardless of whether IrtAB assumes an OF[occl] or OF[open] conformation (Fig. 7).

Spin-labeled IrtAB purified in LMNG was measured under three conditions: (i) WT-IrtAB, apo; (ii) WT-IrtAB in the presence of ATP-Mg and MBT and (iii) 2xEQ-IrtAB in the presence of ATP-Mg. For the intracellular pair, we observed distance shortening of the 2xEQ-IrtAB/ATP-Mg sample with respect to the WT-IrtAB/apo sample (Fig. 7), which indicates complete NBD dimerization and intracellular gate closure. In contrast, in the presence of ATP-Mg and Fe-MBT (i.e., under turnover conditions), we observed only minor changes with respect to the apo-state peak, indicating a prevalent inward-facing conformation with separated NBDs. Curiously, our cryo-EM analyses suggested a strong population of the OF[occl] conformation under basically identical turnover conditions, showing that cryo-EM and DEER analyses can lead to different conclusions. Potential reasons for such discrepancies are different freezing conditions and the introduction of spin labels in the case of DEER experiments, which may have both influenced the conformational space of IrtAB.

For the two extracellular pairs, we did not observe any sign of distance change that would indicate periplasmic gate opening (Fig. 7). Hence, the DEER measurements support a transport cycle of IrtAB that alternates between IF and OF[occl] conformations but does not sample the OF[open] conformation.

IrtAB is highly asymmetric

When comparing the IF and OF[occl] structures of IrtAB by dissecting them according to transmembrane helix (TMH) bundles moving as rigid bodies in type IV ABC transporters (Supplementary Fig. 21), we observed that the most prominent structural

Fig. 7 | DEER analysis of IrtAB. a Spin-labeling positions are shown between intracellular pair N305C[IrtB]-S221C[IrtB] (green) and extracellular pairs S51C[IrtB]-S153C[IrtB] (blue) or A362C[IrtA]-T579C[IrtA] (orange) for cryo-EM structures (IF and OF[occl] conformation) or a homology model based on the OF[open] TM287/288 structure. IrtA is colored teal, and IrtB is magenta, and cysteines are shown as spheres. Dotted lines connect the thiol-groups. **b** Distances between nitroxide spin-labels (MTSSL) were simulated based on cryo-EM structures (for IF and OF[occl] conformation, shaded gray and red areas, respectively) or the homology model (shaded blue) shown in (**a**). Measured distance distributions are shown as solid lines. The distance distributions and their corresponding uncertainties (shown as gray-shaded areas around the curves corresponding to a 95 % confidence bound) were determined using a neural network analysis (ref. 53).
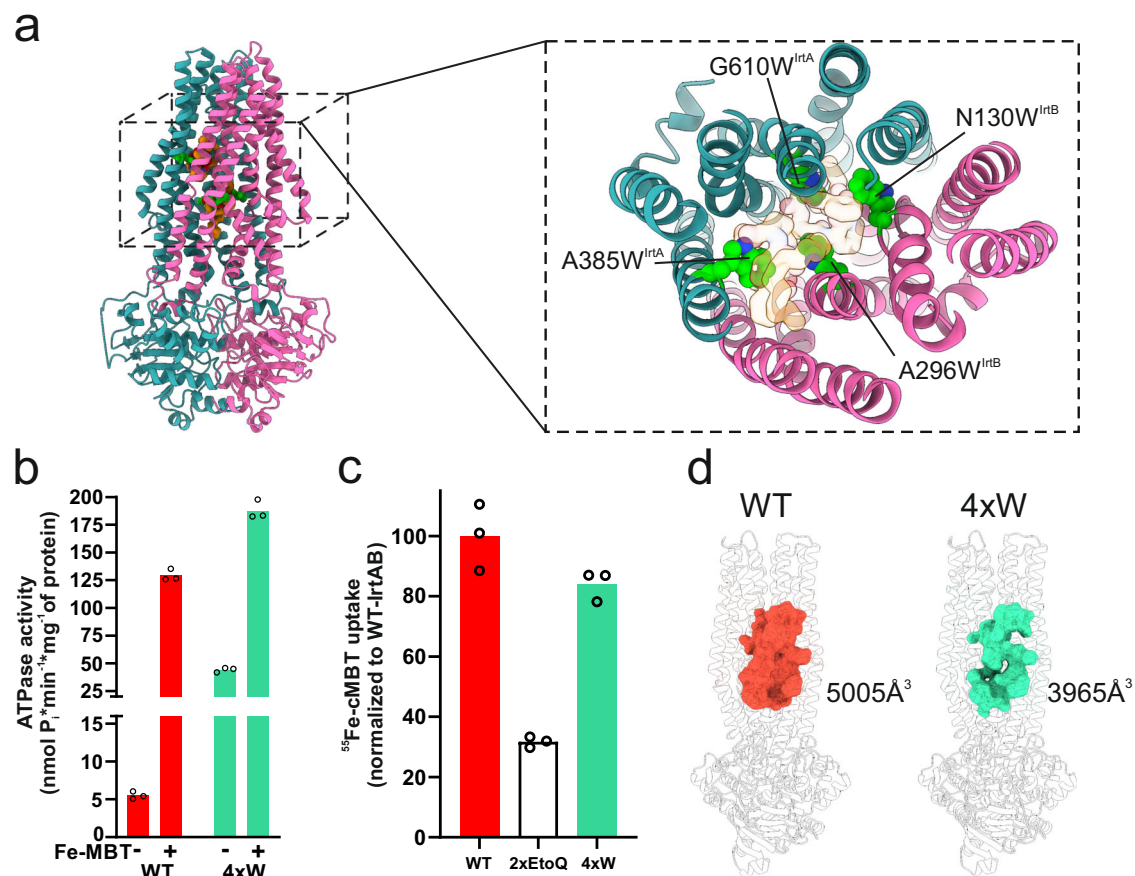
Fig. 8 | Analysis of cavity mutations. a Model of OF$_{occl}$ IrtAB wherein four small cavity residues were mutated to tryptophane (4xW-IrtAB). **b** ATPase activity of purified 4xW-IrtAB with WT-IrtAB as the control in the presence or absence of 5 μM MBT. Data points correspond to technical quadruplicates. **c** In vivo uptake of ^{55}Fe-cMBT in *M. smegmatis* cells unable to produce their own siderophores and lacking the genomic copy of *irtAB*. Cells were complemented with WT-IrtAB (positive control), ATPase-deficient 2xEQ-IrtAB (negative control), and 4xW-IrtAB. Note that *M. smegmatis* cells exhibit IrtAB-independent Fe-cMBT uptake. Data points correspond to technical triplicates. **b, c** For both functional assays, representative data of at least two biological replicates are shown. Source data are provided as a Source Data file. **d** Side-by-side comparison of the occluded cavity of WT-IrtAB (experimental structure) and 4xW-IrtAB (model).

rearrangements occur in the domain swap helices TMH4-5 of IrtA and IrtB, which differ by RMSD values of 2.7 Å and 4.6 Å, respectively. These RMSD values go way beyond what is observed for analogous rigid body movements of any other type IV ABC transporter of known structure undergoing the IF to OF$_{occl}$ transition (Supplementary Fig. 22). Overall, the conformational transition of IrtAB is highly asymmetric (Supplementary Fig. 21) and is associated with unusually strong rotation of the NBDs (Supplementary Fig. 23), which underpin the inability of IrtAB to assume an outward-facing conformation. Of note, previous type IV ABC transporter structures have revealed functionally relevant α-helical breaks in the TMH4-5 region, namely for *C. elegans* ABCB1[27] and Cyanidioschyzon merolae ABCB1[28]. Another notable example is a break of TMH4 of *E. coli* MsbA caused by the inhibitor G907[29]. Finally, inward-facing YbtPQ features a coil-to-helix transition in TMH4 of YbtP upon yersiniabactin binding[21].

Size reduction of the occluded cavity does not impact mycobactin import

To assess whether the outward-occluded cavity of IrtAB is directly involved in mycobactin import, we decreased its volume by introducing four bulky tryptophane residues into the cavity wall (4xW-IrtAB). Intriguingly, 4xW-IrtAB retained its capacity to import mycobactin in the radioactive cMBT uptake assay (Fig. 8), providing indirect evidence that mycobactin does not pass through the central cavity of IrtAB.

Discussion

Our data suggest that IrtAB most likely catalyzes the import of Fe-MBT via a credit-card mechanism (Fig. 9), wherein the transporter provides a hydrophilic groove for the polar substrate head group and shields it during translocation, and the lipophilic part remains embedded in the lipid bilayer[30,31]. We provide here direct experimental evidence that Fe-MBT binds to the outside of the TMDs of IrtAB (state 2 in Fig. 9). Since the structure was determined in nanodiscs, Fe-MBT must have penetrated the lipid bilayer to reach the observed mycobactin binding site. The prominent membrane-facing crevice at the IrtA/IrtB interface constitutes the most plausible pathway for Fe-MBT translocation. In strong support of this notion, we identified two mutations placed at the crevice or directly at the mycobactin binding site, which both prevent mycobactin import without affecting protein folding. Structural analyses of these variants revealed that they result in the collapse of the membrane-facing crevice.

How Fe-MBT continues its journey from the middle of the membrane to the cytoplasm leaves room for alternative interpretations. One possibility is a trap-and-flip mechanism, wherein mycobactin would first enter the large internal cavity of outward-occluded IrtAB. Transition to the inward-facing conformation would then release mycobactin to the inner leaflet of the cytoplasmic membrane[15,32,33], where it can be reduced by the SID to release Fe^{2+}[8] (transition via states 3a and 3b in Fig. 9). This translocation route would require further opening of the membrane-facing crevice to provide access of
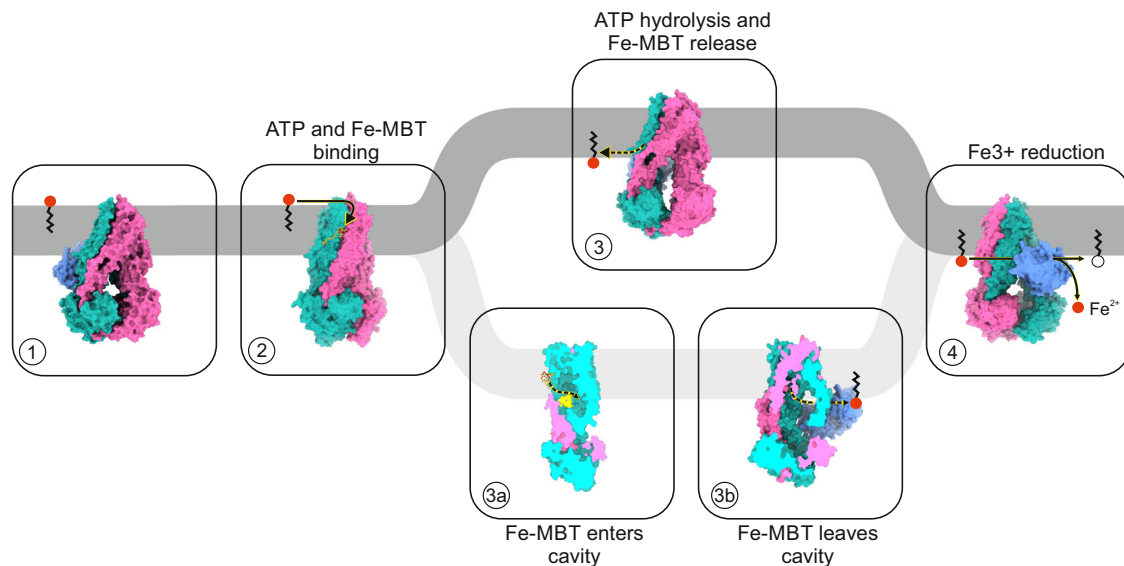
Fig. 9 | Proposed mycobactin import and reduction mechanism of IrtAB. Fe-MBT is shown as a red dot with a lipid tail or as a chemical structure shown in orange sticks. The membrane is depicted as a gray bar. The SID is colored blue, IrtA teal, and IrtB magenta. Descriptions are provided in the main text.

mycobactin to the large cavity, which is, considering the size of the mycobactin head group, not plausible. Further, the 4xW-IrtAB variant retains transport activity (Fig. 8) even with its four bulky tryptophane residues pointing into the cavity, which speaks against a trap-and-flip mechanism.

In a more likely scenario, the path of mycobactin continues at the outside of IrtAB's TMDs (transition via state 3 in Fig. 9). The crevice collapses when the transporter transits to its inward-facing conformation (Fig. 2), thereby squeezing the bound mycobactin towards the cell interior. Concomitantly, TMH5^{IrtB} breaks and thereby provides space for the mycobactin head group to reach the cytosol. In the structure of 3xHtoA-IrtAB, the conformation of the loop connecting the broken helices of TMH5^{IrtB} is altered (Fig. 6). It is plausible to assume that alterations in this region prevent Fe-MBT release when IrtAB transits to its inward-facing conformation, thereby explaining why 3xHtoA-IrtAB lacks transport activity. One may also speculate that this region only permits Fe-MBT passage when the HHH-motif is complexed with a zinc ion, though we do not provide structural evidence for this notion in this work.

Our suggested route of transport shares analogies to credit-card mechanisms described for scramblases[34,35], with the notable difference that the credit-card swipe is split into two parts and that conformational changes invoked by ATP binding and hydrolysis are required to push the head group of the substrate towards the cytosol. In support of this notion, ATPase deficient 2xEQ-IrtAB is heavily impaired in mycobactin import. Among ABC transporters, IrtAB shares commonalities with PglK, a type IV ABC transporter responsible for the flipping of lipid-linked oligosaccharides in bacteria[36]. PglK was suggested to flip its amphiphilic substrate by catalyzing the translocation of the polar head group while the lipidic moiety remains embedded in the lipid bilayer without trapping the entire substrate in the central TMD cavity. Other aspects of the transport mechanism, however, differ between IrtAB and PglK, namely the direction of transport (import versus export) and the conformations required to drive transport (i.e., alternating between OF$_{occl}$ and IF conformations for IrtAB and between OF$_{occl}$ and OF$_{open}$ conformations for PglK).

A remarkable biochemical observation of our study is the identification of three uncoupled IrtAB variants (Q249R^{IrtB}, A256R^{IrtB}, and 3xHtoA). In purified form, these variants exhibit basal ATPase activities, which can be further stimulated by Fe-MBT, suggesting that they are still capable of sensing Fe-MBT. At the same time, these

variants completely lack transport activity, owing to structural changes in the membrane-facing crevice as discovered in three corresponding cryo-EM structures. This raises the question about the molecular mechanism by which Fe-MBT triggers ATP hydrolysis. Since we have not found a variant whose basal activity is similarly low as WT-IrtAB, but which cannot be longer stimulated by Fe-MBT, there must be an unidentified binding site responsible for Fe-MBT sensing. Another recurrent pattern was the elevation of the basal ATPase activity for many studied variants. Especially Q249A^{IrtB}, Q249L^{IrtB}, and Q249F^{IrtB} cannot be further stimulated by Fe-MBT. Curiously, these fully stimulated variants still import Fe-MBT, suggesting that they wastefully hydrolyze ATP in the absence of available Fe-MBT, but are not strongly affected when it comes to Fe-MTB transport itself. In other words, the residues lining the membrane-facing crevice of WT-IrtAB, and in particular Q249^{IrtB}, strongly suppress the basal ATPase activity, and thereby allow for the capacity to strongly stimulate ATPase activity when Fe-MBT is present.

Conceptually, it would be rather simple to convert an ABC exporter to an ABC importer. Namely, the OF$_{open}$ conformation would need to encompass a high-affinity binding pocket for the substrate, which would collapse when the transporter transits to the IF conformation, thereby resulting in substrate release inside the cell. Indeed, inversion of transport directionality has been observed for several single mutants of EfrCD to import Hoechst instead of exporting it ref. [37], as well as for ABCB1 carrying 14 alanine substitutions in the TMDs exhibiting drug import activity[38]. For IrtAB, however, we were unable to detect the OF$_{open}$ conformation in our cryo-EM and DEER measurements. Instead, we provide here evidence for a transport mechanism that functions by alternating between the IF and OF$_{occl}$ conformation (Fig. 9). As shown by dissecting IrtAB into structural elements typically moving as rigid bodies in type IV ABC transporters (Supplementary Fig. 21), the most dramatic conformational distortions occur at the domain swap helices TMH4^{IrtB} and TMH5^{IrtB}, which are broken in the IF conformation and straighten during the IF to OF$_{occl}$ transition. These are exactly the key conformational changes that finally establish the lateral crevice at the IrtA/IrtB interface, thereby forming an alternative periplasmic gate for mycobactins that strikingly differs from the canonical gate opening as first observed for Sav1816 and being the hallmark of the OF$_{open}$ conformation[17,26,39]. Of note, even in the closely related OF$_{occl}$ structure yersiniabactin importer YbtPQ[20], the crevice is not apparent (Supplementary Fig. 16), suggesting that

IrtAB's import route might be unique among siderophore importers of the same fold.

We discovered that IrtAB harbors a highly conserved Zn^{2+}-binding site that is required to couple ATP hydrolysis to active import. Our data suggest that zinc coordination fulfills a regulatory role, likely at the release step when IrtAB transits to its inward-facing conformation (transition via step 3 in Fig. 9). The binding affinity of the HHH-motif for Zn^{2+} was found to be in the double-digit nanomolar range, thus allowing for exchange with free zinc present within the cell. In a physiological context, the HHH-motif might ensure that IrtAB-mediated Fe-(c)MBT uptake only takes place when there is enough zinc present in the cell. Transcriptome and proteome analyses of *M. tuberculosis* have revealed several layers of cross-signaling between zinc and iron uptake systems, with the ESX-3 secretion machinery playing a key role for both micronutrients[40–42]. Mediated by transcriptional regulators, zinc uptake in *Aspergillus fumigatus* was found to be dependent on iron availability under zinc-replete conditions, thereby preventing a toxic imbalance of iron and zinc[43]. Iron and zinc are both essential constituents for co-factors of enzymes and biomolecules playing a role in electron transport chains, but they become toxic when taken up in excess, in particular in the case of free intracellular Fe^{2+} catalyzing the Fenton reaction[44]. During the infection cycle of mycobacteria, the invading pathogen is confronted with highly divergent Zn^{2+}/Fe^{3+} ratios. While iron availability is limited at all times, the zinc concentration varies from low in the blood and in the mycobacteria-specific case, where it is scavenged by calprotectin, to very high in the macrophage phagosome, where bursts of zinc are released to intoxicate mycobacteria[45]. To counteract these bursts, mycobacteria upregulate detoxifying Zn^{2+} exporters belonging to the family of P-type ATPases, that organize into metal efflux platforms[46]. These mechanisms coordinating the uptake of iron and zinc operate at the transcriptional level and are, therefore, comparatively slow. By contrast, the zinc-binding site we discovered in IrtAB might provide a much faster reaction to respond to sudden changes in Zn^{2+}/Fe^{3+} ratios. Why and in which physiological contexts this rapid regulation mechanism is crucial will be subject to future studies.

Methods

Strains, media, constructs, and cloning

E.coli MC1061 was used for cloning and expression of proteins. Cloning and expression precultures were performed in Luria Broth (LB) liquid medium or LB agar plates. For protein expression in *E. coli*, terrific broth (TB) was used. For mycobactin and carboxymycobactin production, *M. smegmatis* mc²155 wild-type and *M. smegmatis* *ΔfxbC* strains were used, respectively. For radioactive uptake experiments, *M. smegmatis ΔfxbAΔmbtDΔirtAB* (TKO) complemented with the respective IrtAB variant was used. For mycobacterial cultures in rich medium, 7H9 with OADC supplement was used for liquid cultures and 7H10 with OADC supplement for agar plates. Low-iron minimal medium for the production of mycobactins was prepared exactly as described previously[8]. Antibiotics used for protein expression and cloning in *E.coli* were ampicillin 100 μg/ml, chloramphenicol 25 μg/ml, and apramycin 50 μg/ml. When working with *M. smegmatis*, apramycin was used at a concentration of 25 μg/ml.

M. thermoresistible irtAB previously cloned into the pINIT vector[8] was used for the generation of point mutants (Q249L^{IrtB}, Q249F^{IrtB}, Q249R^{IrtB}, Q249A^{IrtB}, A256L^{IrtB}, A256F^{IrtB}, A256R^{IrtB}) with primer pairs listed in Supplementary Table S2. Cystein-free IrtAB was created by mutating the native C199A^{IrtA} by using primer pair #16. Afterwards, DEER labeling pairs N305C^{IrtB}-S221C^{IrtB}, S51C^{IrtB}-S153C^{IrtB}, A362C^{IrtA}-T579C^{IrtA} were introduced into cysteine-free IrtAB, by using primer pairs #17-#18, #19-#20, #21-#22, respectively, in two separate quickchange cloning reactions. The Walker B mutations E815Q^{IrtA} and E493Q^{IrtB} to obtain a 2xEQ-IrtAB background were introduced on the three existing cysteine pair mutants using primer pairs #23 and #24 in two separate cloning steps. For the functional analysis of the triple histidine motif, single mutations H393A^{IrtA}, H439A^{IrtA}, and H444A^{IrtA} were introduced with primer pairs #8, #9, and #10, respectively. The 3xHtoA mutant was created on IrtAB-H393A^{IrtA} with primer pair #11 introducing both H439A^{IrtA} and H444A^{IrtA} mutations. For the structural analysis of the 3xHtoA mutant, the truncated 3xHtoA devoid of the SID was cloned from the pINIT vector by using primers #25 and #26-rev. 4xW-IrtAB mutant was created with subsequent quickchange reactions using primers #12-#15 in Table S2.

For protein expression, pBXC3GH (Addgene #47070) plasmid was used to express GFP-tagged protein for ICP-MS measurements, fluorescent titrations, and nanodisc reconstitution to generate datasets #1, #2, #5, and #6. For ATPase assays and structure determination in LMNG (datasets #3-4 and #9-11), the pBXC3H (Addgene #47068) plasmid was used, which adds a His-tag at the C-terminus of IrtB. For radioactive $^{55}Fe^{3+}$-cMBT uptake assays in *M. smegmatis ΔfxbAΔmbtDΔirtAB*, point mutants were subcloned from pINIT vectors into the mycobacterial complementation vector pFLAG (Addgene #110095)[47].

Protein expression and purification

Proteins were produced in and purified from *E. coli* MC1061 using a TB medium containing 100 μg/ml ampicillin. Cells were inoculated 1:50 from an overnight LB culture and grown for 2 h at 37 °C while shaking in baffled flasks. After temperature adjustment to 25 °C over 1 h, expression was induced with 0.02 % (w/v) L-arabinose for overnight expression. Cells were collected by centrifugation at 9000 × g for 15 min at 4 °C. The pellet was resuspended in TBS (20 mM Tris-HCl pH 7.5, 150 mM NaCl) containing DNase I (Thermo Scientific). Resuspended cells were lysed with a Microfluidizer M-110P (Microfluidics) with three passes at 25 kPa. The lysate was first centrifuged for 30 min at 8000 × g at 4 °C to remove cell debris, and the supernatant was further centrifuged at 170'000 g to pellet membrane fraction (Beckman-Colter). The pelleted membrane vesicles were resuspended in TBS buffer, flash-frozen, and stored at − 80 °C until further use.

IrtAB-specific sybody SybNL5 was previously selected as crystallization chaperone[8,48]. SybNL5 was expressed in the pBXNPHM3 vector overnight. Cells were collected and lysed with a microfluidizer, then the remaining cell debris was removed by low-spin centrifugation. Lysate was purified over a Ni-NTA column and eluted protein-MBP complex was cleaved with 3 C enzyme during dialysis. His-tagged MBP and 3 C enzyme were removed by reapplying the sample on a Ni-NTA column. The flow-through was concentrated and further purified by size exclusion chromatography (SEC) on a Superdex 200 Increase 10/300 GL (GE Healthcare) column. As SybNL5 did not hinder the ATPase activity of IrtAB (Supplementary Fig. 2h), it was used as fiducial marker datasets #1 and #9-11.

Depending on the experimental use, IrtAB was either purified via C-terminal His-tag with Ni^{2+}-affinity chromatography or via C-terminal GFP-tag with in-house prepared GFP-nanobody (PDB 3K1K) resin. For structure determination in detergent-solubilized samples and ATPase assays, membrane vesicles were thawed and solubilized in 1.3 % β-DDM for 2 h during head-over rotation. Solubilized membrane proteins were separated by 30 min ultracentrifugation at 170'000 g. The supernatant was supplemented with 20 mM imidazole and loaded onto Ni-NTA resin (Qiagen) for batch-binding at 4 °C for at least an hour with gentle stirring. Subsequently, the resin was washed on a column with 20 column volumes (CV, typically 100 ml) wash buffer (50 mM imidazole pH 7.5, 200 mM NaCl, 10% glycerol, and 0.01 % LMNG). IrtAB was eluted with 2 CV elution buffers (200 mM imidazole, pH 7.5, 200 mM NaCl, 10 % glycerol, and 0.01% LMNG). The eluted protein was concentrated to 1–3 mg/ml and 560 μl aliquots were frozen for subsequent separation by SEC in TBS buffer supplemented with 0.01 % (w/v) LMNG

for ATPase assays, datasets #3-4 or 0.005 % (w/v) LMNG for datasets #7-11.

For cryo-EM analyses in nanodisc, IrtAB was purified as described above, but only β-DDM (0.03 %, w/v) was used during Ni-affinity purification and the first round of SEC (0.03 %, w/v). Then, IrtAB was reconstituted into nanodiscs as previously described[8] with minor modifications as follows. For samples of datasets #1-2, IrtAB:MSP1-D1E3:lipids ratio of 1:8:240 was used, whereas for datasets #5 and #6, a very tight nanodisc with 1:3:90 ratio was assembled. After removal of Bio-Beads (SM-2, Bio-Rad), reconstituted IrtAB was cleaved by 3 C enzyme and subsequently concentrated using a 100 kDa cut-off filter (Amicon). This way, most of the cleaved GFP, 3 C enzyme, and empty nanodiscs were removed from the sample prior to size-exclusion chromatography. The nanodiscs-reconstituted protein was finally separated on a Superose 6 Increase 10/300 GL column (GE Healthcare) in TBS buffer and peak fractions were pooled and concentrated for subsequent cryo-EM sample preparation in nanodisc.

For samples analyzed by ICP-MS and preparations for zinc affinity measurements, WT-IrtAB and 3xHtoA-IrtAB were purified via the C-terminal GFP-tag to avoid potential metal contamination. GFP-affinity purification was performed by in-house prepared beads coated with NHS immobilized GFP-nanobody (PDB 3K1K). DDM-solubilized membrane vesicles were incubated with GFP-resin overnight at 4 °C with gentle agitation to allow batch-binding. Then, the resin was transferred into an empty column and washed with 20 CV TBS buffer containing 10 % glycerol and 0.03 % β-DDM (w/v). For elution, the resin was loaded onto a 5 mL tube and incubated for 2 h with gentle agitation at 4 °C in the presence of 3 C enzyme (400 µg). Subsequently, the resin was loaded onto an empty column, and cleaved protein was eluted with 2 CV TBS containing 10 % glycerol and 0.03 % β-DDM (w/v). The flow-through was flash-frozen and stored at −80 °C until further use.

Cysteine-labeled IrtAB samples for DEER measurements were expressed and purified as the cryo-EM samples described above, with the exception, that all purification buffers starting with membrane solubilization contained 2 mM DTT. Before MTSL labeling, DTT was removed by desalting on a PD10 column (GE Healthcare), and subsequently, a 5-fold molar excess of MTSL ((1-oxyl-2,2,5,5-tetramethyl-Δ3-pyrroline-3-methyl)methanethiosulfonate, Toronto Research) per cysteine was added for overnight labeling at 4 °C with gentle agitation. Excess of spin label was removed by SEC on a Superose 6 Increase 10/300 GL (GE Healthcare) column in TBS containing 0.01 % LMNG (w/v). Protein fractions were concentrated and used immediately for sample preparation.

ATPase assay

ATPase activity assay was performed with LMNG solubilized IrtAB as described in our previous work[8] with modifications. In brief, frozen aliquots of Ni-affinity purified MTHERM-IrtAB mutants were thawed and further purified on a Superose 6 Increase 10/300 GL (GE Healthcare) column in TBS containing 0.01 % LMNG. Main peak fractions were pooled, and concentration was adjusted to a concentration of 3−60 nM, depending on the basal or stimulated activity of each mutant, in order to reach phosphate levels detected in the linear range of the assay. Mutants were incubated at 37 °C for 15 min with 2.5 mM ATP or 1.25 mM ATP and 10 mM MgSO4 in TBS supplemented with 0.01 % LMNG, in the presence or absence of 5 µM MBT. ATPase stimulation of LMNG solubilized IrtAB with MBT and cMBT was performed with 15 nM protein and was incubated for 60 min at 37 °C. For read-out, malachite green-molybdate solution was added as described previously to detect the release of inorganic phosphate by measuring the absorbance at 650 nm[49,50]. Buffer control was used for background subtraction. The assays were performed with technical triplicates or quadruplicates and in biological duplicates and representative data is shown.

Radioactive uptake assay

^{55}Fe-cMBT uptake was measured in vivo as described previously[8], with minor modifications. Strains were grown to stationary phase in iron-rich 7H9 medium, then inoculated 1:50 in iron-depleted minimal medium and grown to OD_{600} 2.5-5. Before the experiment, OD_{600} was adjusted to the lowest OD_{600} of all strains in the experiment. For variants Q249L^{IrtB}, Q249F^{IrtB}, Q249R^{IrtB}, Q249A^{IrtB}, A256L^{IrtB}, A256F^{IrtB}, A256R^{IrtB}, and triple histidine motif variants H393A^{IrtA}, H439A^{IrtA}, H444A^{IrtA} and 3xHtoA, three aliquots of 0.5 ml of each culture (technical triplicates) were put on ice. To each aliquot, radioactively labeled ^{55}Fe-cMBT, dissolved in a minimal medium, was added to reach a final concentration of around 10 µM. While still on ice, for each variant, 3 x 200 µl culture was filtered and washed on a 96-well vacuum manifold using a glass fiber filtermat, thus measuring background binding values as technical triplicates. Then, the bacterial cultures were transferred to a 37 °C heating block and incubated while shaking at 1000 rpm. 30-minute end-point measurements were performed the same way as the background time points. Kinetic measurement for 3xHtoA mutant was performed from 1 ml bacterial culture by taking 200 µl samples at each time point. Accumulated radioactive ^{55}Fe-cMBT was quantified with MicroBeta2 scintillation counter (Perkin Elmer), by using a MeltiLex-B solid scintillator sheet melted onto the glass fiber filter sheet.

Siderophore production, desferration and radioactive labeling

Mycobactins used for structure determination and functional assays, were produced, extracted, and radioactively labeled exactly as described before[8].

Metal analysis with ICP-MS sample preparation and analysis

For samples analyzed by ICP-MS, frozen aliquots of GFP-tag purified WT-IrtAB and 3xHtoA-IrtAB were further purified by size exclusion chromatography (SEC) on a Superose 6 Increase 10/300 (GE Healthcare) column in TBS supplemented with 0.03 % β-DDM. Protein fractions corresponding to IrtAB were pooled and concentrated to 4 µM. For initial metal content analysis, untreated WT-IrtAB as well as SEC buffer were extracted by adding 1 ml HNO3 (60 %, Merck 1.01518.1000, for trace analysis) and 1 ml H2O2 (30 %, Merck, for trace analysis) in a sonication bath at 40 °C for 1 h. The volume was adjusted to 4 ml with 2 % HNO3 solution prior to ICP-MS analysis.

ICP-MS measurements were performed with an Agilent QQQ 8800 Triple quad ICP-MS spectrometer, equipped with a standard x-lens setting, nickel cones, and a "micro-mist" quartz nebulizer. The feed was 0.1 ml/min, and the RF power was 1550 W. Tune settings were based on the Agilent General Purpose method and only slightly modified by an autotune procedure using an Agilent 1 ppb tuning solution containing Li, Y, Ce, Tl, and Co (Agilent). Values are reported as the average of 30 sweeps x 3 replicates. Elements were measured without gas as well as with He and H2 as collision gases. All solutions were prepared from 60 % HNO3 (Merck 1.01518.1000 ultrapure) and 18.2 MΩ Millipore water.

For the metal saturation experiment, concentrated protein samples were divided into three aliquots. Each aliquot was incubated with either 200 µM ZnSO4, 200 µM NiSO4, or SEC buffer for control. After 30 min of incubation on ice, the samples were split into two technical replicates and desalted on PD midiTrap G-25 (Cytiva) columns. The protein concentration of the flow-through was measured on a Nano-Drop 2000c (Thermo Scientific), and the samples were sent for quantitative ICP-MS metal analysis to determine the amount of bound metals. Extraction and ICP-MS analyses were carried out as above with the additional step that external calibration curves were recorded using a serial dilution made from ICP multi-element standard solution IV (Merck 1.11355.0100) in 2 % HNO3. Zinc and nickel quantification was performed based on single-charged ions and was limited to the following isotopes: ^{58}Ni, ^{60}Ni, ^{66}Zn, and ^{68}Zn. The metal saturation experiment was performed in biological duplicates starting from

protein purification, and representative technical duplicates of a biological replicate are shown.

Zinc affinity measurement

For zinc affinity measurements, frozen aliquots of GFP-tag purified WT-IrtAB or 3xHtoA-IrtAB were thawed and gel filtrated on a Superose 6 Increase 10/300 (GE Healthcare) column in TBS supplemented with 0.03 % β-DDM. Peak fractions were pooled and used directly for competition assays. WT-IrtAB, 3xHtoA-IrtAB, or EGTA were added to the mixture with 200 nM FluoZin-3, at a final concentration of 200 nM. The mixture was titrated with $Zn(NO_3)_2$ standard solution (1000 mg/l, Supelco) in 5–500 nM steps up to 10 uM concentration while stirring at 900 rpm. Temperature was set to 25 °C and the interval between each titration step was 50 s. Zinc saturation on FluoZin-3 was monitored by the change in fluorescence by LS-55 florescence spectrometer (Perkin Elmer). The excitation wavelength was set to 494 nm, and emission was detected at 516 nm, with 10 nm slit-width for both.

Fluorescence data points for WT- and 3xHtoA-IrtAB were derived from the titration curve, by averaging the fluorescence value of final 30 s of each titration step and plotting it against the Zn^{2+} concentration. For EGTA competition, data points are the average of three single florescence readouts after each titration step.

For plotting, the data points (F_i) were normalized against the minimum (F_{min}) and maximum (F_{max}) fluorescence ($F_{norm} = (F_i − F_{min})/(F_{max} − F_{min})$). F_{norm} points were plotted against Zn^{2+} concentration and fitted by least square fit using the Hill equation ($F_{norm} = B_{max}[Zn^{2+}]\hat{~}h/(EC_{50}\hat{~}h + [Zn^{2+}]\hat{~}h)$) in GraphPad Prism, where h is the Hill slope and B_{max} is the maximum specific binding and EC_{50} corresponds to the Zn^{2+} concentration at which $F_{norm} = 0.5*B_{max}$. Fluorescence titrations were performed in a single biological replicate.

DEER sample preparation and analysis

Inter-spin distance distribution predictions were performed with a rotamer-based approach in MMM[25,51] and used to choose suitable positions for the labeling. DEER samples were prepared using detergent-purified, MTSL-labeled IrtAB at a final concentration of 20 μM in TBS buffer supplemented with 0.01% LMNG. 10% glycerol-d_8 (Sigma Aldrich) was added as a cryoprotectant to each sample and a final sample volume of 40 μl was frozen in liquid nitrogen. For the WT-IrtAB sample under turnover conditions, additionally 2.5 mM ATP, 2.5 mM $MgCl_2$, and 20 μM MBT were added, whereas the spin-labeled samples prepared on the 2xEQ-IrtAB background were supplemented with 2.5 mM ATP and 2.5 mM $MgCl_2$. The ATPase activity of purified, spin-labeled IrtAB was highly similar to WT-IrtAB, both in the presence and absence of Fe-MBT.

DEER measurements were performed at 50 K on a Bruker ELEXSYS E580Q-AWG (arbitrary waveform generator) dedicated pulse Q-band spectrometer equipped with a 150 W TWT amplifier and a homemade resonator[52]. A 4-pulse DEER sequence with Gaussian, non-selective observer and pump pulses of 32 ns length (corresponding to 13.6 ns FWHM) with 100 MHz frequency separation was used. The pump position was always chosen as the maximum of the nitroxide signal. DEER experiments were performed using the dead-time free 4-pulse DEER sequence $(\pi/2)_{obs}$-(d1)-$(\pi)_{obs}$-(d1+T)-$(\pi)_{pump}$-(d2-T)-$(\pi)_{obs}$-(d2)-(echo) with a 16-step phase cycling. The initial value of the interpulse delay t_1 was set to 400 ns. Deuterium ESEEM was suppressed by incrementing t_1 eight times by 16 ns and summing the individual traces (nuclear modulation averaging). The shot repetition time (SRT) was set to 3 ms. Data were analyzed using the latest version of DEERNet[53] available for Spinach[54]. Raw DEER data are shown (Supplementary Fig. 24).

Cryo-EM sample preparation

For the sample recorded as dataset #1, 5 mM ATP-γ-S, 5 mM MgCl2, and 1.5 molar excess of SybNL5 were added to nanodisc reconstituted full-length WT-IrtAB (15 μM) prior to blotting. The sample was blotted on a glow-discharged QuantiFoil R1.2/1.3 Au 200 grid for 2.5–3.5 s at 10 °C in 90% relative humidity, then frozen in liquid ethane in a Leica GP2 plunge-freezer.

Orthovanadate-trapped nanodisc sample yielding dataset #2 was reconstituted as described above, but the lipid mixture was spiked with 50 μM Fe-MBT before incubation with Bio-Beads. Prior to blotting, 2.5 mM ATP, 2.5 mM $MgCl_2$, and 5 mM orthovanadate were added to nanodiscs-reconstituted full-length WT-IrtAB (15 μM). Orthovanadate solution was preheated at 98 °C for 10 min before addition to the sample. Then, the sample was blotted on a glow-discharged QuantiFoil R1.2/1.3 Cu 200 grid for 2.5–3.5 s and plunged into liquid ethane on a Leica GP2 plunge-freezer.

LMNG solubilized full-length WT-IrtAB (20 μM) giving rise to dataset #3 was frozen without additives. The sample was blotted on a glow-discharged QuantiFoil R 1.2/1.3 Au 200 mesh for 3-4 s and plunged in liquid ethane on a Leica GP2 plunge-freezer at 11 °C and 70% relative humidity.

Sample of dataset #4 contained LMNG solubilized full-length WT-IrtAB (20 μM), which was frozen upon adding 100 μM Fe-MBT, 2.5 mM ATP, 2.5 mM $MgCl_2$ and 5 mM orthovanadate. The sample was frozen on glow discharged QuantiFoil R 1.2/1.3 Au 200 mesh grids and blotted for 3-4 s and plunged in liquid ethane on a Leica GP2 plunge-freezer operated at 10 °C and 95% relative humidity.

ATP-trapped, nanodiscs-reconstituted 2xEQ-IrtABΔSID with or without Fe-MBT (dataset #5 and #6, respectively) were plunged on QuantiFoil R1.2/1.3 Au 300 grids, blotted for 5.5-6 s at 4 °C in 100% relative humidity and frozen in liquid ethane-propane mixture using a Vitrobot IV Mark plunge-freezer (Thermo Fisher Scientific). Grids of dataset #5-11 were glow-discharged under a 39 Pa air atmosphere, at 15 mA current for 60 s with a Pelco easiGlow glow-discharger (Ted Pella). Mycobactin containing sample (dataset #5) was pre-incubated with 20 μM Fe-ATP for 5 min on ice, then prior to plunging, 5 mM ATP-Mg was added, and the sample and incubated at 25 °C for 30 s. A control sample was handled the same way, except for the addition of Fe-MBT (dataset #6).

LMNG-purified 2xEQ-IrtABΔSID containing additionally the Q249R[IrtB] or A256R[IrtB] substitutions (datasets #7 and #8, respectively), were plunged on glow-discharged QuantiFoil R1.2/1.3 Au 300 grids, blotted for 5.5-6 s at 4 °C in 100% relative humidity using a Vitrobot IV Mark plunge-freezer (Thermo Fisher Scientific). Before plunging, 20 μM mycobactin and 5 mM ATP-Mg were added to the samples and preincubated at 25 °C for 30 s.

For the turnover samples, WT-IrtABΔSID (datasets #9 and #10) or 3xHtoA- IrtABΔSID (dataset #11) were purified in TBS supplemented with 0.005% LMNG, and 1.5 molar excess of SybNL5 was added to form a complex before the final size-exclusion step. The peak fractions corresponding to the IrtAB-SybNL5 complex were pooled and concentrated to 20 μM. Prior to blotting, each sample was preincubated for 30 s at 25 °C in a thermocycler in the presence of 2 mM ATP, 2 mM $MgCl_2$, and either 20 μM mycobactin (datasets #9 and #11) or no substrate as control (dataset #10). Turnover samples were dispensed on glow-discharged QuantiFoil R1.2/1.3 Au 300 grids and blotted for 5-6 s (blotting force 20) at 4 °C and 100% relative humidity, then freeze in liquid ethane-propane mixture, using a Vitrobot Mark IV (Thermo Fisher Scientific) plunge-freezer.

Cryo-EM data collection and processing

Datasets #1-6 and #9-11 were collected on a Titan Krios G3i (Thermo Fisher Scientific) operated at 300 kV. Micrographs were recorded with a 100 μm objective aperture and a post-column BioQuantum energy filter with a 20 eV slit and a K3 direct electron detector (Gatan) in super-resolution mode at a nominal magnification of 130,000 ×. Movies in datasets #1-4 were saved without binning with a physical pixel size of 0.65 Å (0.325 Å in super-resolution mode) and datasets #5-

6 and #9-11 were collected with 2-times binning within EPU, allowing for faster data collection, with a pixel size of 0.65 Å in super-resolution mode in LZW-compressed file format. Datasets #7-8 were collected on Glacios 2 equipped with Falcon 4i detector (Thermo Fisher Scientific) operated at 200 kV. Micrographs were recorded with 100 μm objective aperture without an energy filter at a nominal magnification of 190'000x. Movies of these two datasets were saved with a physical pixel size of 0.72 Å in LZW-compressed TIFF file format. Data acquisition was automatized with EPU v2.9-v3.6 (Thermo Fisher). Data acquisition parameters (total dose and defocus range) are listed for each dataset in Supplementary Table 1.

Movies of datasets #1-4 were corrected for beam-induced motion in MotionCor2 and simultaneously binned to 0.65 Å pixel size. Motion-corrected micrographs were imported into CryoSPARC v3.0, v3.1, or v3.2 (dataset #1-2, dataset #4 and dataset #3, respectively) for processing. CTF values were estimated with the Patch CTF method and micrographs were rejected based on relative ice thickness, full frame motion, and estimated CTF resolution. The initial volume for template picking was generated on a smaller subset of particles by blob picking. Template-picked particles were extracted with binning and purified in silico through several rounds of 2D classification. Clean particles were subjected to ab initio reconstruction and reconstructions with promising features were subjected to heterogeneous refinement to further classify particles in 3D. Finally, maps showing defined, high-resolution features were refined using a non-uniform refinement algorithm with global CTF refinements correcting for beam-tilt[55].

Turnover datasets #5-11 were fully processed in CryoSPARC v3.2-v4.5. Pre-processing of movies was performed on the fly win CryoSPARC Live, and generously template-picked particles were extracted. Large amounts of particles were purified in silico with 2D classification, then bona fide particles were subjected to ab initio reconstruction, several rounds of heterogeneous refinements, and finally non-uniform refinement with global CTF refinements correcting for data collection with beam tilt. In the case of datasets #6-8, conformational heterogeneity was further resolved with 3D classification, and final classes were refined with non-uniform algorithm.

3D Variability Analysis (3DVA) of WT-IrtAB in LMNG (dataset #3) was performed in cryoSparc v3.3.1[56]. The final set of particles from the last non-uniform refinement was used to solve 5 modes filtered at 6 Å resolution. The mode resolving the SID swinging movement was displayed in linear mode with 20 frames.

Model building and refinement
The IF model was built based on the crystallographic model of IrtAB (PDB: 6TEJ) and was fitted into the cryo-EM maps of dataset #1 with Dock in Map tool in Phenix. After visual inspections in Coot the model was polished in ISOLDE[57]. This model was then used for model building of the other IF structures. The OF$_{occl}$ models were initially built manually in Coot by using the inward-facing IrtAB crystal structure as a template and finally polished in ISOLDE. Mg^{2+}, Zn^{2+}, waters, and other ligands such as ATP-γ-S, ADP, and ATP were added from the CCP4 monomer library in Coot and fine-tuned in ISOLDE. Geometry restraints for ADP-orthovanadate ligands were generated in the eLBOW tool of Phenix based on isomeric SMILES from the AOV monomer listed in the Ligand Expo ligand library[58]. The initial 3D structure of Fe-MBT was built using the Molefacture module in VMD[59]. The initial structure was energy-minimized for 2000 steepest descent steps. Then, Fe-MBT was placed in a POPE membrane and was equilibrated for 100 ns using Gromacs[60]. A few snapshots from the end of equilibration were taken and converted into the CIF format. One of the snapshots, fitting the EM density the best, was used for the final modeling by generating geometry restraints on the Grade2 v1.6.0 webserver (Global Phasing). For ADP-orthovanadate and Fe-MBT, the polishing step in ISOLDE was skipped since vanadate and iron were not supported by the force field. Before deposition, each model was refined in real space in Phenix against the final maps of the respective datasets.

Structure analysis
RMSD and distance calculations were performed in Chimera v1.15 and ChimeraX v1.5. Figures were prepared in ChimeraX v1.5-8[61–63]. Cavity volumes were calculated by a locally implemented 3 V Voss Volume Voxelator, using a 9 Å outer probe radius and an inner probe radius of 1.87 Å, which corresponds to the size of a single methyl group to visualize lipid accessible space[64,65]. SID movements were visualized and calculated from the 3DVA. The angle was calculated by fitting the crystallographic model of the SID (PDB ID: 6TEK) in the first and last frames and measuring rotation between the fitted models in ChimeraX. Conformational state distribution analysis was performed by ab initio reconstruction of bona fide particles with 5 classes because the differences between IF and OF$_{occl}$ particles can be discerned at this low resolution.

Docking of mycobactin molecules in the cavity was performed with the Autodock Vina tool within Chimera v1.15 using default parameters[66]. Iron(III)-bound *M. smegmatis* mycobactin was drawn in MarvinSketch (Chemaxon https://www.chemaxon.com)) from the isomeric SMILES on PubChem (CID: 135499491). The model of IrtAB and mycobactin was prepared for docking with the Dock Prep tool with default settings, and with the exception of mycobactin, the charge assignment was performed with Gasteiger parameters.

Reporting summary
Further information on research design is available in the Nature Portfolio Reporting Summary linked to this article.

Data availability
Structural models have been deposited to the Protein Data Bank (PDB) with the accession codes 9FXC, 9G2K, 9G2L, 9G2M, 9FW3, 9G2P, 9G2S, 9G2T, 9GL3, 9G2V, 9G2X, 9G2Y, 9G2Z, 9G36 and 9G37. The cryo-EM data has been deposited in the Electron Microscopy Data Bank (EMDB) with the accession codes EMDB-50848, EMDB-50977, EMDB-50978, EMDB-50979, EMDB-50820, EMDB-50980, EMDB-50982, EMDB-50983, EMDB-51435, EMDB-50985, EMDB-50987, EMDB-50988, EMDB-50989, EMDB-50992 and EMDB-50993. Plasmids and other data that support the findings of this study are available from the corresponding authors upon request. Source data are provided in this paper.

References
1. Kurthkoti, K. et al. The capacity of mycobacterium tuberculosis to survive iron starvation might enable it to persist in iron-deprived microenvironments of human granulomas. *Mbio* **8**, e01092–17 (2017).
2. Ratledge, C. Iron, mycobacteria and tuberculosis. *Tuberculosis* **84**, 110–130 (2004).
3. Ratledge, C. & Ewing, M. The occurrence of carboxymycobactin, the siderophore of pathogenic mycobacteria, as a second extracellular siderophore in Mycobacterium smegmatis. *Microbiology* **142**, 2207–2212 (1996).
4. Wells, R. M. et al. Discovery of a siderophore export system essential for virulence of Mycobacterium tuberculosis. *Plos Pathog.* **9**, e1003120 (2013).
5. Zhang, L. et al. Comprehensive analysis of iron utilization by Mycobacterium tuberculosis. *Plos Pathog.* **16**, e1008337 (2020).
6. Jones, C. M. et al. Self-poisoning of Mycobacterium tuberculosis by interrupting siderophore recycling. *Proc. Natl. Acad. Sci. USA* **111**, 1945–1950 (2014).
7. Rodriguez, G. M. & Smith, I. Identification of an ABC transporter required for iron acquisition and virulence in Mycobacterium tuberculosis. *J. Bacteriol.* **188**, 424–430 (2006).

8. Arnold, F. M. et al. The ABC exporter IrtAB imports and reduces mycobacterial siderophores. *Nature* **580**, 413–417 (2020).

9. Lewinson, O., Orelle, C. & Seeger, M. A. Structures of ABC transporters: handle with care. *FEBS Lett.* **594**, 3799–3814 (2020).

10. Ryndak, M. B., Wang, S. S., Smith, I. & Rodriguez, G. M. The Mycobacterium tuberculosis high-affinity iron importer, IrtA, contains an FAD-binding domain. *J. Bacteriol.* **192**, 861–869 (2010).

11. Rodriguez, G. M., Voskuil, M. I., Gold, B., Schoolnik, G. K. & Smith, I. ideR, an essential gene in Mycobacterium tuberculosis: Role of IdeR in iron-dependent gene expression, iron metabolism, and oxidative stress response. *Infect. Immun.* **70**, 3371–3381 (2002).

12. Thomas, C. et al. Structural and functional diversity calls for a new classification of ABC transporters. *FEBS Lett.* **594**, 3767–3775 (2020).

13. Sun, S. et al. Cryo-EM structures for the Mycobacterium tuberculosis iron-loaded siderophore transporter IrtAB. *Protein Cell* 2023 **14**, 448–458 (2023).

14. Choudhury, H. G. et al. Structure of an antibacterial peptide ATP-binding cassette transporter in a novel outward occluded state. *Proc. Natl. Acad. Sci. USA* **111**, 9145–9150 (2014).

15. Mi, W. et al. Structural basis of MsbA-mediated lipopolysaccharide transport. *Nature* **549**, 233 (2017).

16. Galazzo, L. et al. The ABC transporter MsbA adopts the wide inward-open conformation in E. coli cells. *Sci. Adv.* **8**, eabn6845 (2022).

17. Hofmann, S. et al. Conformation space of a heterodimeric ABC exporter under turnover conditions. *Nature* **571**, 580–583 (2019).

18. Fan, C. & Rees, D. C. Glutathione binding to the plant AtAtm3 transporter and implications for the conformational coupling of ABC transporters. *Elife* **11**, e76140 (2022).

19. Lin, D. Y., Huang, S. & Chen, J. Crystal structures of a polypeptide processing and secretion transporter. *Nature* **523**, 425–430 (2015).

20. Hu, W., Parkinson, C. & Zheng, H. Mechanistic insights revealed by YbtPQ in the occluded state. *Biomolecules* **14**, 322 (2024).

21. Wang, Z. M., Hu, W. X. & Zheng, H. J. Pathogenic siderophore ABC importer YbtPQ adopts a surprising fold of exporter. *Sci. Adv.* **6**, eaay7997 (2020).

22. Rulíšek, L. R. & Vondrášek, J. Coordination geometries of selected transition metal ions (Co^{2+}, Ni^{2+}, Cu^{2+}, Zn^{2+}, Cd^{2+}, and Hg^{2+}) in metalloproteins. *J. Inorg. Biochem.* **71**, 115–127 (1998).

23. Lee, B. C., Chu, T. K., Dill, K. A. & Zuckermann, R. N. Biomimetic nanostructures: creating a high-affinity zinc-binding site in a folded nonbiological polymer. *J. Am. Chem. Soc.* **130**, 8847–8855 (2008).

24. Gee, K. R., Zhou, Z. L., Qian, W. J. & Kennedy, R. Detection and imaging of zinc secretion from pancreatic beta-cells using a new fluorescent zinc indicator. *J. Am. Chem. Soc.* **124**, 776–778 (2002).

25. Polyhach, Y., Bordignon, E. & Jeschke, G. Rotamer libraries of spin labelled cysteines for protein studies. *Phys. Chem. Chem. Phys.* **13**, 2356–2366 (2011).

26. Hutter, C. A. J. et al. The extracellular gate shapes the energy profile of an ABC exporter. *Nat. Commun.* **10**, 2260 (2019).

27. Jin, M. S., Oldham, M. L., Zhang, Q. & Chen, J. Crystal structure of the multidrug transporter P-glycoprotein from Caenorhabditis elegans. *Nature* **490**, 566–569 (2012).

28. Kodan, A. et al. Structural basis for gating mechanisms of a eukaryotic P-glycoprotein homolog. *Proc. Natl. Acad. Sci. USA* **111**, 4049–4054 (2014).

29. Ho, H. et al. Structural basis for dual-mode inhibition of the ABC transporter MsbA. *Nature* **557**, 196–201 (2018).

30. Arndt, M. et al. Structural basis for the activation of the lipid scramblase TMEM16F. *Nat. Commun.* **13**, 6692 (2022).

31. Roland, B. P. & Graham, T. R. Decoding P4-ATPase substrate interactions. *Crit. Rev. Biochem. Mol. Biol.* **51**, 513–527 (2016).

32. Lambert, E., Mehdipour, A. R., Schmidt, A., Hummer, G. & Perez, C. Evidence for a trap-and-flip mechanism in a proton-dependent lipid transporter. *Nat. Commun.* **13**, 1022 (2022).

33. Martinez-Molledo, M., Nji, E. & Reyes, N. Structural insights into the lysophospholipid brain uptake mechanism and its inhibition by syncytin-2. *Nat. Struct. Mol. Biol.* **29**, 604 (2022).

34. Falzone, M. E. et al. Nimigean, and A. Accardi, Structural basis of Ca-dependent activation and lipid transport by a TMEM16 scramblase. *Elife* **8**, e43229 (2019).

35. Paulino, C., Kalienkova, V., Lam, A. K. M., Neldner, Y. & Dutzler, R. Activation mechanism of the calcium-activated chloride channel TMEM16A revealed by cryo-EM. *Nature* **552**, 421–425 (2017).

36. Perez, C. et al. Structure and mechanism of an active lipid-linked oligosaccharide flippase. *Nature* **524**, 433 (2015).

37. Meier, G. et al. Deep mutational scan of a drug efflux pump reveals its structure-function landscape. *Nat. Chem. Biol.* **19**, 440–450 (2023).

38. Sajid, A. et al. Reversing the direction of drug transport mediated by the human multidrug transporter P-glycoprotein. *Proc. Natl. Acad. Sci. USA* **117**, 29609–29617 (2020).

39. Dawson, R. J. & Locher, K. P. Structure of a bacterial multidrug ABC transporter. *Nature* **443**, 180–185 (2006).

40. Serafini, A., Pisu, D., Palù, G., Rodriguez, G. M. & Manganelli, R. The ESX-3 secretion system is necessary for iron and zinc homeostasis in Mycobacterium tuberculosis. *PLoS ONE* **8**, e78351 (2013).

41. Siegrist, M. S. et al. Mycobacterial Esx-3 is required for mycobactin-mediated iron acquisition. *Proc. Natl. Acad. Sci. USA* **106**, 18792–18797 (2009).

42. Dow, A. et al. Zinc limitation triggers anticipatory adaptations in Mycobacterium tuberculosis. *PLoS Pathog.* **17**, e1009570 (2021).

43. Vicentefranqueira, R., Leal, F., Marin, L., Sanchez, C. I. & Calera, J. A. The interplay between zinc and iron homeostasis in Aspergillus fumigatus under zinc-replete conditions relies on the iron-mediated regulation of alternative transcription units of zafA and the basal amount of the ZafA zinc-responsiveness transcription factor. *Environ. Microbiol.* **21**, 2787–2808 (2019).

44. Winterbourn, C. C. Toxicity of iron and hydrogen peroxide: the Fenton reaction. *Toxicol. Lett.* **82-83**, 969–974 (1995).

45. Botella, H. et al. Mycobacterial P-1-Type ATPases mediate resistance to zinc poisoning in human macrophages. *Cell Host Microbe* **10**, 248–259 (2011).

46. Boudehen, Y. M. et al. Mycobacterial resistance to zinc poisoning requires assembly of P-ATPase-containing membrane metal efflux platforms. *Nat. Commun.* **13**, 4731 (2022).

47. Arnold, F. M. et al. A uniform cloning platform for mycobacterial genetics and protein production. *Sci. Rep.* **8**, 9539 (2018).

48. Zimmermann, I. et al. Synthetic single domain antibodies for the conformational trapping of membrane proteins. *Elife* **7**, e34317 (2018).

49. Timachi, M. H. et al. Exploring conformational equilibria of a heterodimeric ABC transporter. *ELife* **6**, e20236 (2017).

50. Hohl, M. et al. Structural basis for allosteric cross-talk between the asymmetric nucleotide binding sites of a heterodimeric ABC exporter. *Proc. Natl. Acad. Sci. USA* **111**, 11025–11030 (2014).

51. Jeschke, G. MMM: A toolbox for integrative structure modeling. *Protein Sci.* **27**, 76–85 (2018).

52. Tschaggelar, R. et al. Cryogenic 35GHz pulse ENDOR probehead accommodating large sample sizes: Performance and applications. *J. Magn. Reson.* **200**, 81–87 (2009).

53. Worswick, S. G., Spencer, J. A., Jeschke, G. & Kuprov, I. Deep neural network processing of DEER data. *Sci. Adv.* **4**, eaat5218 (2018).

54. Hogben, H. J., Krzystyniak, M., Charnock, G. T. P., Hore, P. J. & Kuprov, I. Spinach – A software library for simulation of spin dynamics in large spin systems. *J. Magn. Reson.* **208**, 179–194 (2011).

55. Punjani, A., Zhang, H. & Fleet, D. J. Non-uniform refinement: adaptive regularization improves single-particle cryo-EM reconstruction. *Nat. Methods* **17**, 1214–1221 (2020).

56. Punjani, A. & Fleet, D. J. 3D variability analysis: Resolving continuous flexibility and discrete heterogeneity from single particle cryo-EM. *J. Struct. Biol.* **213**, 107702 (2021).

57. Croll, T. I. ISOLDE: a physically realistic environment for model building into low-resolution electron-density maps. *Acta Crystallogr. Sect. D Struct. Biol.* **74**, 519–530 (2018).

58. Moriarty, N. W., Grosse-Kunstleve, R. W. & Adams, P. D. electronic Ligand Builder and Optimization Workbench (eLBOW): a tool for ligand coordinate and restraint generation. *Acta Crystallogr. Sect. D Biol. Crystallogr.* **65**, 1074–1080 (2009).

59. Humphrey, W., Dalke, A. & Schulten, K. VMD: Visual molecular dynamics. *J. Mol. Graph. Model.* **14**, 33–38 (1996).

60. Abraham, M. J. et al. GROMACS: High performance molecular simulations through multi-level parallelism from laptops to supercomputers. *SoftwareX* **1-2**, 19–25 (2015).

61. Pettersen, E. F. et al. UCSF Chimera—A visualization system for exploratory research and analysis. *J. Comput. Chem.* **25**, 1605–1612 (2004).

62. Goddard, T. D. et al. UCSF ChimeraX: Meeting modern challenges in visualization and analysis. *Protein Sci.* **27**, 14–25 (2018).

63. Pettersen, E. F. et al. UCSF ChimeraX: Structure visualization for researchers, educators, and developers. *Protein Sci.* **30**, 70–82 (2021).

64. Voss, N. R. & Gerstein, M. 3V: cavity, channel and cleft volume calculator and extractor. *Nucleic Acids Res.* **38**, W555–W562 (2010).

65. Kawabata, T. & Go, N. Detection of pockets on protein surfaces using small and large probe spheres to find putative ligand binding sites. *Proteins Struct. Funct. Bioinf.* **68**, 516–529 (2007).

66. Trott, O. & Olson, A. J. AutoDock Vina: Improving the speed and accuracy of docking with a new scoring function, efficient optimization, and multithreading. *J. Comput. Chem.* **31**, 455–461 (2010).

Acknowledgements

Author contributions

I.G., F.M.A., and M.A.S. conceived the project. I.G. generated IrtAB variants, prepared all IrtAB samples, collected datasets #5-11, and performed data processing and model building for all datasets. A.R.M. generated the model for Fe-MBT. I.G. and N.P.L. performed ATPase activity and radioactive uptake assays. I.G. established and performed the ICP-MS measurements for metals and the fluorescent zinc binding assay. S.S. collected datasets #1-4 and provided cryo-EM training for I.G. L.G. performed DEER measurements with samples prepared by IG. All authors discussed the results. I.G. and M.A.S. wrote the paper. L.G., N.P.L., and E.B. edited the paper.

Competing interests

The authors declare no competing interests.

Additional information

Supplementary information The online version contains supplementary material available at https://doi.org/10.1038/s41467-024-55136-7.

Correspondence and requests for materials should be addressed to Enrica Bordignon or Markus A. Seeger.

Peer review information *Nature Communications* thanks Damian Ekiert, and the other anonymous reviewer(s) for their contribution to the peer review of this work. A peer review file is available.

Reprints and permissions information is available at http://www.nature.com/reprints

Publisher's note Springer Nature remains neutral with regard to jurisdictional claims in published maps and institutional affiliations.